Aerosol retrievals from the ACEPOL Campaign

Guangliang Fu[1], Otto Hasekamp[1], Jeroen Rietjens[1], Martijn Smit[1], Antonio Di Noia[2], Brian Cairns[3], Andrzej Wasilewski[4], David Diner[5], Feng Xu[5], Kirk Knobelspiesse[6], Meng Gao[6], Arlindo da Silva[6], Sharon Burton[7], Chris Hostetler[7], John Hair[7], and Richard Ferrare[7]

[1]Netherlands Institute for Space Research (SRON, NWO-I), Utrecht, The Netherlands.
[2]University of Leicester.
[3]NASA Goddard Institute for Space Studies (GISS).
[4]Trinnovim LLC.
[5]NASA Jet Propulsion Laboratory (JPL).
[6]NASA Goddard Space Flight Center.
[7]NASA Langley Research Center.

Correspondence: Guangliang Fu (g.fu@sron.nl), Otto Hasekamp (o.hasekamp@sron.nl)

Abstract.

In this paper, we present aerosol retrieval results from the ACEPOL (Aerosol Characterization from Polarimeter and Lidar) campaign, which was a joint initiative between NASA and SRON - Netherlands Institute for Space Research. The campaign took place in October-November 2017 over the western part of the United States. During ACEPOL six different instruments were deployed on the NASA ER-2 high altitude aircraft, including four Multi-Angle Polarimeters (MAPs): SPEX airborne, the Airborne Hyper Angular Rainbow Polarimeter (AirHARP), the Airborne Multi-angle SpectroPolarimeter Imager (AirMSPI), and the Research Scanning Polarimeter (RSP). Also, two lidars participated: the High Spectral Resolution Lidar -2 (HSRL-2) and the Cloud Physics Lidar (CPL). Flights were conducted mainly for scenes with low aerosol load over land but also some cases with higher AOD were observed. We perform aerosol retrievals from SPEX airborne, RSP (410-865 nm range only), and AirMSPI using the SRON aerosol retrieval algorithm and compare the results against AERONET and HSRL-2 measurements (for SPEX airborne and RSP). All three MAPs compare well against AERONET for the Aerosol Optical Depth (AOD) (Mean Absolute Error (MAE) between 0.014-0.024 at 440 nm). For the fine mode effective radius the MAE ranges between 0.021-0.028 micron. For the comparison with HSRL-2 we focus on a day with low AOD (0.02-0.14 at 532 nm) over the California Central Valley, Arizona and Nevada (26 October) and a flight with high AOD (including measurements with AOD > 1.0 at 532 nm) over a prescribed forest fire in Arizona (9 November). For the day with low AOD the MAE in AOD (at 532 nm) with HSRL-2 are 0.014 and 0.022 for SPEX and RSP, respectively, showing the capability of MAPs to provide accurate AOD retrievals for the challenging case of low AOD over land. For the retrievals over the smoke plume also a reasonable agreement in AOD between the MAPs and HSRL-2 was found (MAE 0.088 and 0.079 for SPEX and RSP, respectively), despite the fact that the comparison is hampered by large spatial variability in AOD throughout the smoke plume. Also a good comparison is found between the MAPs and HSRL-2 for the aerosol depolarization ratio (a measure for particles sphericity) with MAE of 0.023 and 0.016 for SPEX and RSP, respectively. Finally, SPEX and RSP agree very well for the retrieved microphysical and optical properties of the smoke plume.

1 Introduction

Aerosols such as smoke, sulphate, dust, and volcanic ash particles affect the Earth climate directly by interaction with radiation and indirectly by modifying the cloud properties. In contrast to the warming effect of greenhouse gases, which is understood quite well, the quantification of aerosol cooling contains a large uncertainty, as reported in the latest (5th) assessment report of the Intergovernmental Panel on Climate Change (IPCC, 2014). This large uncertainty adds substantial difficulties in the prediction of the Earth's climate change in future. Aerosols also have a big influence on air quality. Air pollution from aerosols may result in severe adverse problems to human health (Wyzga and Rohr, 2015). To improve our understanding of the aerosol effect on climate and air quality, accurate global measurements of aerosol optical properties (e.g., aerosol optical depth (AOD), single scattering albedo (SSA)), microphysical properties (size distribution, refractive index, particles shape), and their vertical distribution, are of crucial importance. Satellite instruments are needed to obtain such measurements at a global scale.

Lidar measurements are needed to obtain vertical profile information about aerosols. The Cloud-Aerosol Lidar with Orthogonal Polarization (CALIOP) elastic backscatter Lidar (Winker et al., 2010), has been providing aerosol Lidar measurements since 2006. High Spectral Resolution Lidar (HSRL) techniques (Hair et al., 2008) are being used for the new generation of Lidar instrumentation such as the Cloud-Aerosol Transport System (CATS) instrument (Yorks et al., 2014), which has been operational on the International Space Station (ISS) in the period 2015-2017, and for the European Space Agency (ESA) Earthcare mission (Illingworth et al., 2014), expected for launch in 2021. In comparison to elastic backscatter lidars, the HSRL technique has an additional filtered channel that provides an assessment of aerosol extinction. It also improves the accuracy of the aerosol backscatter profile, especially at altitudes far from the instrument, since it is calculated as a direct ratio of two channels instead of retrieved with assumptions that result in accumulating errors. The HSRL methodology also improves the aerosol depolarization through the improved backscatter and provides the aerosol lidar ratio using the extinction (Burton et al., 2012).

From a passive remote sensing point-of-view, instruments that measure both intensity and polarization and observe a ground pixel under multiple viewing angles contain the richest set of information about aerosols in our atmosphere (Dubovik et al., 2019). This has been demonstrated by a number of studies on synthetic measurements (Mishchenko and Travis, 1997; Hasekamp and Landgraf, 2007; Hasekamp, 2010; Knobelspiesse et al., 2012), airborne measurements (Chowdhary et al., 2005; Waquet et al., 2009; Xu et al., 2017; Wu et al., 2015, 2016), and spaceborne measurements (Hasekamp et al., 2011; Dubovik et al., 2011; Fu and Hasekamp, 2018).

The best known satellite instruments that performed multi-angle photopolarimetric measurements of the Earth atmosphere were the POLDER (Polarization and Directionality of the Earth's Reflectances) instruments (Deschamps et al., 1994), of which the recently decommissioned POLDER-3 on board the PARASOL micro-satellite provided data from 2005-2013. Although the original algorithms for aerosol retrieval from POLDER-3 do not make full use of the information contained in the MAP measurements (Deuzé et al., 2000, 2001), algorithms developed more recently (Dubovik et al., 2011; Hasekamp et al., 2011; Fu and Hasekamp, 2018) do fully exploit the available information and provide insight in the capabilities and limitations of the POLDER-3 instrument. The advanced data products of these algorithms have been applied at global (Lacagnina et al., 2015,

2017) and regional (Chen et al., 2018) scale. The main limitation of the POLDER instruments is the limited accuracy with which the Degree of Linear Polarization (DoLP) can be measured. The DoLP accuracy is intrinsically limited by the filter wheel technology, which relies on sequential measurements of different polarization directions, in combination with a spatial under-sampling. On the other hand, the advantage of this technology is that it allows for a large swath with (almost) global
5   coverage in a day.

Driven by the need for daily global coverage for the Copernicus Atmospheric Monitoring Service (CAMS, https:// atmosphere.copernicus.eu/), the POLDER design also forms the blueprint for the 3MI instruments (Fougnie et al., 2018), to be flown on METOP-SG in the time frame ∼2020-2035. 3MI uses the same filter-wheel technology - with the corresponding DoLP accuracy - but has more spectral bands than POLDER, including bands in the Short Wave Infra-Red (SWIR), albeit
10   with reduced angular range.

Focus for the development of new polarimetric instrumentation has been on improved polarimetric accuracy, more viewing angles, more wavelengths, an extended spectral range, or a combination of these aspects. For a number of these instrument concepts airborne demonstrators for possible future satellite missions have been built: 1) the Research Scanning Polarimeter (RSP) (Cairns et al., 2004) which is an airborne version of the Aerosol Polarimetry Sensor (APS) (Mishchenko et al., 2007)
15   that was lost in a failed launch in 2011. RSP measures at many viewing angles (∼150) and 9 wavelength bands between 410-2250 nm. It has a demonstrated DoLP accuracy of better than 0.002 (Knobelspiesse et al., 2019). 2) The Airborne Multiangle SpectroPolarimetric Imager (AirMSPI) (Diner et al., 2013). AirMSPI is an eight-band (355, 380, 445, 470, 555, 660, 865, 935 nm) pushbroom camera, measuring polarization in the 470, 660, and 865 nm bands, mounted on a gimbal to acquire multiangular observations over a $\pm 67°$ along-track range. The AirMSPI concept will be implemented in a satellite mission
20   as the Multi-Angle Imager for Aerosols (MAIA) to be launched in ∼2021 (Diner et al., 2018). 3) The Airborne Hyper-Angular Rainbow Polarimeter (AirHARP) (Martins et al., 2018). AirHARP is a wide field-of-view imager that measures in the spectral bands at 440, 550, 670, and 865 nm where 670 nm is measured under 60 and the other bands under 20 viewing geometries. This concept will be implemented in a satellite instrument for a Cubesat mission to be launched in 2019 and for the Phytoplankton Aerosol Cloud and ocean Ecosystems (PACE) mission, to be launched 2022 (Werdell et al., 2019). 4) The
25   Spectro-polarimeter for Planetary Exploration (SPEX airborne) instrument (Smit et al., 2019). SPEX airborne employs the spectral modulation technique (Snik et al., 2009) to accurately measure the DoLP with a spectral resolution of 10-20 nm. The intensity is being measured at higher spectral resolution of 2-3 nm. SPEX airborne performs multi-angle measurements at 9 viewing angles ranging between $\pm 56°$ in a spectral range between 400-800 nm. The SPEX concept will be implemented in a satellite instrument SPEXone (Hasekamp et al., 2019) for the NASA PACE mission (Werdell et al., 2019).
30   All 4 airborne MAPs listed above were mounted on the NASA Earth Resources-2 (ER-2) high altitude aircraft (Navarro, 2007) during the Aerosol Characterization from Polarimeter and Lidar (ACEPOL) campaign, which was performed from October-November 2017, starting from the NASA Armstrong airbase in Palmdale, California. During ACEPOL, also two lidars were deployed on the ER-2: the High Spectral Resolution Lidar-2 (HSRL-2) (Hair et al., 2008), providing vertically resolved measurements of backscatter coefficients (at 355, 532, and 1064 nm), extinction coefficients (at 355 and 532 nm), and

depolarization ratio (at 355, 532, and 1064 nm) and the Cloud Physics Lidar (CPL) (McGill et al., 2002), providing vertically resolved measurements of backscatter coefficients at 355, 532, and 1064 nm and depolarization ratio at 1064 nm.

The goals of the ACEPOL campaign include: (i) comparison of level-1 (radiance and DoLP) performance between the different MAPs, (ii) comparison of aerosol retrievals from the different MAPs, (iii) comparing MAP retrievals to lidar retrievals,

5 and (iv) performing combined retrievals using both MAP and lidar measurements. The focus of this paper is on aspects (ii) and (iii): We will perform aerosol retrievals from RSP, SPEX airborne, and AirMSPI measurements during ACEPOL, and evaluate the retrievals against AERONET and against HSRL-2. Note that aerosol retrievals from AirHARP measurements are not included in this paper, because the data were not available when performing the here presented analysis.

In this study, we evaluate the performance of the different MAPs for retrieving aerosol optical and microphysical properties,

10 and also their capabilities to provide lidar related aerosol properties. The retrieved aerosol properties are compared and validated with the data from AERONET and HSRL-2. The paper is organized as follows. Section 2 introduces the methodologies of the SRON algorithm for polarimetric aerosol retrievals, section 3 describes the data sets from the ACEPOL campaign, which are used in this study, and the retrievals of different MAPs from ACEPOL are performed and compared with AERONET and HSRL-2 in section 4. Finally, the last section summarizes and concludes this study.

2 Methodology

2.1 SRON multimode retrieval algorithm

In this paper, we employ the SRON aerosol retrieval algorithm in multi-mode setup (Fu and Hasekamp, 2018), for an aerosol size distribution described by 5 modes (see Table 1). We consider mode 1-3 together as the fine mode and mode 4 and 5 together as the coarse mode. To account for spectral dependence, we describe the refractive index m for the fine and coarse mode as

20 $m(\lambda) = \sum_{k=1}^{n} \alpha_k m^k(\lambda)$ where $m^k(\lambda)$ are prescribed refractive indices as function of wavelength and α_k are coefficients to be determined in the retrieval (see below). Both real part and imaginary part of refractive indices are represented in this way. Here, we base the spectral dependence of the refractive index of the standard types of D'Almeida et al. (1991) (Inorganic/Sulphate, Black Carbon, and Dust). Nonspherical aerosols are described as a size/shape mixture of randomly oriented spheroids (Hill et al., 1984; Mishchenko et al., 1997). We use the Mie/T-matrix-improved geometrical optics database by Dubovik et al. (2006)

25 along with their proposed spheroid aspect ratio distribution for computing optical properties for a mixture of spheroids and spheres. The aerosol parameters included in the retrieval state vector x are the aerosol column numbers for the 5 modes (Table 1), 2 coefficients (Inorganic, Black Carbon) for the fine mode refractive index, 2 coefficients (Inorganic, Dust) for the coarse mode refractive index, the fraction of spherical particles (assumed the same for all modes), and the central height of a Gaussian aerosol height distribution (assumed the same for all modes).

30 For the surface reflection matrix we use (Litvinov et al., 2011; Xu et al., 2017):

$$\mathbf{R}_s(\lambda, \mu_{\text{in}}, \mu_{\text{out}}, \phi_v - \phi_0) = A(\lambda) \left(\frac{(\mu_{\text{in}} \mu_{\text{out}})^{k-1}}{(\mu_{\text{in}} + \mu_{\text{out}})^{1-k}} F(g, \Theta)[1 + R(G)] \right) \mathbf{D} + \alpha \, \mathbf{R}_{\text{pol}} \tag{1}$$

where k is a real number between 0 and 1, and $\mathbf{D}$ is the null matrix except $\mathbf{D}_{11} = 1$. The first part accounts for the bidirectional reflectance distribution function (BRDF) parameterized by the Rahman-Pinty-Verstraete (RPV) model (Rahman et al., 1993) and the second part $\mathbf{R}_{\mathrm{pol}}$ accounts for the polarized BRDF parameterized by a micro-facet model (Maignan et al., 2009). The pairs (θ_0, ϕ_0) and (θ_v, ϕ_v) respectively denote the solar and viewing zenith and azimuth angles. μ_{in} and μ_{out}

5 are respectively the cosines of incoming and outgoing angles. g is the asymmetry parameter of the Henyey-Greenstein phase function $F(g, \Theta)$. Θ is the scattering angle. $1 + R(G)$ is an approximation of the hot spot effect (Rahman et al., 1993), where $G = \sqrt{\tan^2\theta_0 + \tan^2\theta_v - 2\tan\theta_0\tan|\theta_v|\cos(\phi_v - \phi_0)}$. We include A at each measured wavelength, and k, g, and α as fit parameters in the state vector.

The measurement vector $\boldsymbol{y}$ contains the measured radiances (sun normalized) and Degree of Linear Polarization (DoLP)

10 values at the different wavelengths and viewing angles. To retrieve the state vector from the measurements, a damped Gauss-Newton iteration method with Phillips-Tikhonov regularization is employed (Hasekamp et al., 2011; Fu and Hasekamp, 2018). The inversion algorithm finds the solution $\hat{\boldsymbol{x}}$, which solves the minimization-optimization problem,

$$\hat{\boldsymbol{x}} = \min_{\boldsymbol{x}}(||\mathbf{S}_y^{-\frac{1}{2}}(\mathbf{F}(\boldsymbol{x}) - \boldsymbol{y})||^2 + \gamma||\mathbf{W}^{-\frac{1}{2}}(\boldsymbol{x} - \boldsymbol{x}_{\mathrm{a}})||^2). \tag{2}$$

Here, $\mathbf{F}$ is the forward model that simulates the measurement for a given state vector $\boldsymbol{x}$. $\mathbf{F}$ consists of a radiative transfer

15 model (Hasekamp and Landgraf, 2002, 2005; Schepers et al., 2014) that simulates Stokes parameters I, Q, U at the top of the atmosphere for given optical properties (scattering and absorption optical thickness and scattering phase matrix for each vertical layer of the model atmosphere), and a part that computes the optical properties from the aerosol microphysical properties using the tabulated kernels of Dubovik et al. (2006) for a mixture of spheroids and spheres. Since the forward model is nonlinear the inversion problem has to be solved iteratively replacing the forward model in each iteration step by its linear approximation.

20 $\boldsymbol{x}_{\mathrm{a}}$ is the a priori state vector, $\mathbf{W}$ is a weighting matrix that ensures that all state vector parameters range within the same order of magnitude (Hasekamp et al., 2011), and $\mathbf{S}_y$ is the measurement error covariance matrix. The regularization parameter γ in Eq. (2) is chosen optimally (for each iteration) from different values (10 values from 0.1 to 5) by evaluating the goodness of fit using a simplified (fast) forward model. In the SRON aerosol algorithm, the first guess of $\boldsymbol{x}$ is obtained before the full inversion retrieval using a multimode Look-Up Table (LUT), which is based on tabulated RT calculations for each mode. For

25 further details we refer to Fu and Hasekamp (2018).

We use the goodness of fit (χ^2) to decide whether the retrievals have successfully converged:

$$\chi^2 = \frac{1}{n_{\mathrm{meas}}} \sum_{i=1}^{n_{\mathrm{meas}}} \frac{(F_i - y_i)^2}{S_y(i,i)}. \tag{3}$$

Here, n_{meas} is the total number of measurements (multi-angle and multispectral radiance and DoLP) for each pixel. We consider valid retrievals those that achieve a χ^2 smaller than an empirically chosen threshold χ^2_{max}. This filter rejects cases in which

30 the forward model is not able to fit the measurements, e.g., because of cloud-contaminated pixels (Stap et al., 2015, 2016), corrupted measurements (Hasekamp et al., 2011), and cases in which the first guess state vector deviates too much from the truth (Di Noia et al., 2015).

2.2 Fine mode and coarse mode effective radius

According to Eq. (2.53) in (Hansen and Travis, 1974), the effective radius is defined:

$$r_{\text{eff}} = \frac{\int_{r_{\min}}^{r_{\max}} \pi r^3 n(r) dr}{\int_{r_{\min}}^{r_{\max}} \pi r^2 n(r) dr} = \frac{R}{G} \tag{4}$$

where $n(r)dr$ is the number of particles with radius between r and $r+dr$. $r_{\min}$ and $r_{\max}$ are the particle radius for the smallest

5   and largest particles.

In this study, a 5-mode retrieval is used. The effective radius for multiple modes together ($r_{\text{eff}}^{\text{m}}$) is calculated from the different

fixed modes by: $r_{\text{eff}}^{\text{m}} = \dfrac{\sum\limits^{n^{\text{m}}} R_i}{\sum\limits_{n^{\text{m}}} G_i}$ where n^{m} is the number of modes grouped together. For the 5-mode retrievals in this study, we

compute r_{eff} for the fine mode (modes 1-3 together) and and coarse mode (modes 4 and 5 together).

2.3 Aerosol depolarization ratio and aerosol lidar ratio

10   The aerosol lidar properties are related to the aerosol scattering matrix. For some general assumptions ((i) scattering by an assembly of randomly oriented particles each having a plane of symmetry, (ii) scattering by an assembly containing particles and their mirror particles in equal numbers and with random orientations, (iii) Rayleigh scattering with or without depolarization effects), the aerosol scattering matrix has a simplified block-diagnonal structure (Bottiger et al., 1980; Mishchenko, 2014):

$$\mathbf{F}(\Theta) = \begin{bmatrix} F_{11}(\Theta) & F_{12}(\Theta) & 0 & 0 \\ F_{12}(\Theta) & F_{22}(\Theta) & 0 & 0 \\ 0 & 0 & F_{33}(\Theta) & F_{34}(\Theta) \\ 0 & 0 & -F_{34}(\Theta) & F_{44}(\Theta) \end{bmatrix} \tag{5}$$

15   where Θ is the scattering angle and F_{11} is the phase function for total radiance.

The aerosol (linear) depolarization ratio is defined as:

$$\delta_{\text{col}}^{\text{pol}} = \frac{F_{11}(180°) - F_{22}(180°)}{F_{11}(180°) + F_{22}(180°)} \tag{6}$$

which is adpated from Eq. (3) in (Mishchenko et al., 2016). We use Eq. (6) to compute an aerosol depolarization ratio from the aerosol properties of the MAPs and compare this to the vertically integrated value measured by HSRL-2, which is calculated

20   by:

$$\hat{\delta}^{\text{hsrl}}(i) = \frac{\delta^{\text{hsrl}}(i)}{1 + \delta^{\text{hsrl}}(i)}, \qquad \hat{\delta}_{\text{col}}^{\text{hsrl}} = \frac{\sum\limits_{i=0}^{n_{\text{bin}}}(\hat{\delta}^{\text{hsrl}}(i)\,\beta_{\text{b}}^{\text{hsrl}}(i))}{\sum\limits_{i=0}^{n_{\text{bin}}}(\beta_{\text{b}}^{\text{hsrl}}(i))}, \qquad \delta_{\text{col}}^{\text{hsrl}} = \frac{\hat{\delta}_{\text{col}}^{\text{hsrl}}}{1 - \hat{\delta}_{\text{col}}^{\text{hsrl}}}, \tag{7}$$

where $i = 0$ corresponds to the bin closet to the surface, $i = n_{\text{bin}}$ corresponds to the bin closet to the aircraft. The aerosol backscatter coefficient ($\beta_{\text{b}}^{\text{hsrl}}(i)$) for each bin is used as the weighting parameter. $\delta^{\text{hsrl}}(i)$ is first transformed to $\hat{\delta}^{\text{hsrl}}(i)$, which is because $\hat{\delta}^{\text{hsrl}}(i)$ mix linearly like backscatter, but $\delta^{\text{hsrl}}(i)$ does not (Burton et al., 2014).

In our retrieval algorithm we assume that for aerosols the single scattering albedo ω and F_{11} do not depend on altitude. In

5   that case, using ω and $F_{11}(180°)$, we compute the vertically integrated aerosol extinction-to-backscatter ratio, i.e., aerosol lidar ratio for a MAP by:

$$S_{\text{col}}^{\text{pol}} = \frac{4\pi}{\omega \, F_{11}(180°)},\tag{8}$$

which is adpated from Eq. (4) in Lopes et al. (2013). This can be compared to the corresponding value from HSRL-2:

$$S_{\text{col}}^{\text{hsrl}} = \frac{\displaystyle\sum_{i=0}^{n_{\text{bin}}} (\beta_{\text{e}}^{\text{hsrl}}(i))}{\displaystyle\sum_{i=0}^{n_{\text{bin}}} (\beta_{\text{b}}^{\text{hsrl}}(i))}\tag{9}$$

10   which is adapted from Eq. (28) in Stamnes et al. (2018). Here $\beta_{\text{e}}^{\text{hsrl}}(i)$ denotes the extinction coefficient for each bin.

3   Measurements

For this study, we use airborne measurements from 3 different polarimeters (SPEX airborne, RSP, AirMSPI) and one lidar (HSRL-2). Further, we use ground based measurements for validation and re-analysis data as input to our retrieval algorithm. All data are described in this section.

15   ### 3.1   RSP

RSP (Cairns et al., 1999) started to operate on the NASA ER-2 since 2010 and has flown on a number of other airplanes since 2001 (Cairns et al., 2003). Multi-viewing capability over a large along-track angular range and at many viewing angles (~ 150) is obtained using a scanning mirror. Due to the fact that some viewing angles are blocked by the aircraft, the angular range of RSP on the ER-2 is restricted to -40° to 60°. The Stokes parameters Q and U are analyzed in separate refractive telescopes,

20   using Wollaston prisms, followed by dichroic beamsplitters. The RSP instrument is equipped with an in-flight calibration system, and the accuracy for the DoLP is better than 0.002 (Knobelspiesse et al., 2019), providing a benchmark (in DoLP) for other MAPs. Aerosol retrievals from RSP have been performed, amongst others, by Waquet et al. (2009); Wu et al. (2015, 2016); Di Noia et al. (2017); Stamnes et al. (2018); Gao et al. (2019).

A complicating factor for using RSP measurements in aerosol retrievals over inhomogeneous land surfaces is that different

25   viewing angles have different ground pixel size and may look at slightly shifted scenes on the ground. To partly overcome this problem we use (1) the approach of Wu et al. (2015) and construct RSP pixels that represent a 5 km along track running average; (2) the (moving average) approach of Di Noia et al. (2017) to select 10 viewing angles covering a broad viewing angle range (over the total RSP viewing angles) and convolve RSP measurements at each selected angle with an average of 5 angles.

In this sense, although averaged measurements 10 viewing angles are input to the retrieval algorithm, they are constructed from original RSP measurements at 50 angles. In this study, we use 5 wavelengths (410, 469.1, 554.9, 670, and 863.4 nm) for RSP retrievals as Di Noia et al. (2017). It should be noted that theoretically the SWIR bands of RSP 1590 and 2250 nm would provide extra constraints for the characterization of coarse mode aerosols. For the ACEPOL campaign however, we found no

5   improvement by including the SWIR bands, and even slightly worse results (compared to AERONET and HSRL-2) in some cases. A possible explanation is that our assumption that the directional property of surface reflection is spectrally neutral does not hold over the full RSP wavelength range. Another explanation may be that the SWIR channels are affected by gas absorption which we could not perfectly correct for.

3.2 AirMSPI

10   AirMSPI (Diner et al., 2013) started to operate on the NASA ER-2 since October 2010. AirMSPI is an eight-band (355, 380, 445, 470, 555, 660, 865, 935 nm) pushbroom camera, which measures linear polarization in the 470, 660, and 865 nm bands. AirMSPI employs a photoelastic modulator-based polarimetric imaging technique to enable accurate measurements of Degree of Linear Polarization (DoLP) in addition to intensity. The instrument is mounted on a gimbal to acquire multiangular observations in the range of $\pm 67°$. AirMSPI has two principal observing modes: (1) step-and-stare, where $11\,\mathrm{km} \times 11\,\mathrm{km}$

15   targets are observed at a discrete set of view angles with a spatial resolution of $\sim 10\,\mathrm{m}$. (2) continuous sweep, where the camera slews back and forth along the flight track between $\pm 65°$ to acquire wide area coverage (11 km swath at nadir, target length 108 km). The spatial resolution is $\sim 25\,\mathrm{m}$. Aerosol retrievals from AirMSPI have been performed by Xu et al. (2017, 2018, 2019). In this study, only the step-and-stare measurements have been used as they provide a mult-angle-view of the same ground scene. For ACEPOL, AirMSPI was programmed to measure at 9 viewing angles in the step-and-stare mode: 0° (nadir),

20   $\pm 29°$, $\pm 48°$, $\pm 59°$, $\pm 66°$. Radiance measurements are used at all wavelengths except 935 nm and DoLP measurements at all 3 wavelengths. Following Xu et al. (2017), for AirMSPI we aggregate individual ground pixels to $1\,\mathrm{km} \times 1\,\mathrm{km}$ spatial grid in order to be less affected by surface inhomogeneity and its effect on the angular co-registration.

3.3 SPEX airborne

SPEX airborne performed its first (engineering) flight on the ER-2 in 2016. ACEPOL has been the first full science campaign.

25   The instrument employs the spectral modulation technique (Snik et al., 2009) to accurately measure the Degree of Linear Polarization (DoLP) in the spectral range 400-800 nm with a spectral resolution of 10-20 nm, and the intensity at a higher spectral resolution of 2-3 nm. A ground-based version of SPEX has performed upward looking measurements from the ground which have been used to successfully retrieve aerosol microphysical and optical properties by van Harten et al. (2014); Di Noia et al. (2015). SPEX airborne performs multi-angle measurements at 9 viewing angles: $\pm 56°$, $\pm 42°$, $\pm 28°$, $\pm 14°$, and 0°.

30   Smit et al. (2019) performed a comparison between SPEX airborne and RSP for radiance and DoLP measurements at 410, 470, 550, and 670 nm. They found very good agreement between SPEX airborne and RSP at 550 and 670 nm whereas the agreement gets worse towards smaller wavelengths. In this study, we use measurements of radiance and DoLP at 16 wavelengths, (450, 460, 470, 480, 490, 500, 510, 520, 530, 540, 550, 565, 580, 600, 670, and 750 nm). The measurement at each wavelength

represents an average of a 10 nm wide spectral region. We leave out the shortest wavelengths because of less good agreement with RSP, and the wavelengths >750 nm because of order overlap of the grating.

Each SPEX viewport has a moderate swath of ∼ 6 degrees (Smit et al., 2019) in the across-track direction, which translates to a projected field of view from 2.4 km at nadir to 4.5 km at fore and aft viewports when the instrument is operated at the typical altitude of ER-2. Conceptually, the instrument acts as nine separate pushbroom spectrometers, which produce nine overlapping strips of data on the ground. In this way, a multi-angular view is obtained of ground scenes when the aircraft flies over it. The spatial sampling of the L1C product is chosen as 1 km× 1 km (across × along-track), which is driven by the L1B spatial resolution of the outer viewports.

3.4 HSRL-2 data

The NASA Langley HSRL-2 instrument, operational since 2012, is a successor to the NASA Langley airborne HSRL-1 instrument, which was described by Hair et al. (2008); Burton et al. (2012) and validated by Rogers et al. (2009). The HSRL-2 uses the HSRL technique to independently measure aerosol extinction and backscatter at 355 nm (Burton et al., 2018) and 532 nm and the standard backscatter technique to measure aerosol backscatter at 1064 nm (Müller et al., 2014). It is polarization sensitive at all three wavelengths. HSRL-2 measures vertically resolved values for the backscatter coefficient (β) and aerosol depolarization ratio at 355, 532, and 1064 nm (Burton et al., 2015) and the extinction coefficient and AOD at the high-spectral-resolution channels, 355 and 532 nm. HSRL-2 is the first airborne system capable of providing 3 backscatter and 2 extinction measurements, which is important for lidar retrievals of microphysical properties (Müller et al., 2014).

For the ACEPOL flights on the ER-2, the aerosol backscatter coefficient is derived using the HSRL technique at 355 nm and 532 nm and the elastic backscatter technique at 1064 nm and reported at a vertical resolution of 15 m and a horizontal/temporal resolution of 10 seconds (approximately 1-2 km at ER-2 cruise speeds). The aerosol depolarization ratios at all 3 wavelengths are reported at the same resolutions. For ACEPOL, the extinction, AOD, and lidar ratio from the HSRL methodology are not available for many ground pixels. In those cases, the aerosol extinction at 355 nm and 532 nm is derived using the aerosol backscatter and an assumed lidar ratio of 40 sr over land and 20 sr over water, and reported at the backscatter resolution. Where the HSRL method is available for extinction products, they are reported at 150 m vertical resolution and at temporal resolution of 60 s generally and 10 s within smoke plumes.

As with the extinction products, the aerosol AOD is reported using the standard HSRL approach where available and is supplemented by AOD calculated using the sum of the true backscatter times the assumed lidar ratio. The systematic uncertainties on the AOD from the HSRL method is about 0.05 for ACEPOL, whereas the assumed lidar ratio produces systematic uncertainty that is a constant relative fraction (± 50%). Therefore, for the case with high AOD, the uncertainty is smaller when using the HSRL method and we therefore use these products for this case. Conversely, although the uncertainties are fairly high for both products for low AOD, the product using an assumed lidar ratio is expected to have lower uncertainties, and we use these products for the low AOD cases in this paper.

3.5 AERONET data

The multispectral aerosol optical depth (AOD) from the MAP and lidar retrievals is compared with AERONET (AErosol RObotic NETwork) level 1.5 data (Holben et al., 2001) (version 3.0). The data are cloud cleared and quality controlled. The effective radius for fine and coarse modes are validated with AERONET level 1.5 Almucantar Retrieval Inversion Products

5   (Dubovik et al., 2002). The AOD of fine and coarse modes are validated with AERONET level 1.5 spectral de-convolution algorithm (SDA) data (O'Neill et al., 2003). In this paper, data from the 6 following AERONET stations are used for validation: Bakersfield, CalTech, Flagstaff ("USGS_Flagstaff_ROLO"), Fresno_2, Modesto, and Railroad-Valley.

3.6 Re-analysis data

The required meteorological inputs for our retrieval scheme are vertical profiles of humidity, temperature, and pressure. We

10   obtain these information from National Centers for Environmental Prediction (NCEP) reanalysis data (Kalnay et al., 1996). For ozone absorption in retrievals, we use the ozone profiles from Modern-Era Retrospective analysis for Research and Applications, Version 2 (MERRA-2) (Gelaro et al., 2017). The data are interpolated to the specific time and location of a MAP ground pixel.

4 Results

15   We apply the SRON algorithm as described in section 2.1 to measurements of SPEX, RSP, and AirMSPI. In our retrievals we use an ad-hoc representation of the measurement error covariance matrix $\mathbf{S}_y$, where we assume a diagonal matrix for $\mathbf{S}_y$ (i.e. errors are uncorrelated for different wavelengths and viewing angles) with values on the diagonal corresponding to 5 % error on the radiance and 0.005 on DoLP. Although this is a crude assumption that does not reflect a bottom-up estimate taking into account individual error sources, it should be noted that for the chosen inversion approach the most important aspect

20   is the relative dependence between radiance and DoLP errors, because we include a flexible regularization parameter that is determined as part of the retrieval. The same results can be obtained when assuming 2.5 % radiance and 0.0025 DoLP errors, in combination with a different χ^2 filter. This relative dependence between radiance and DoLP accuracies seems reasonable for all three instruments given that they all have a high DoLP accuracy. Another note is that there are error sources such as mis-registration between different viewing angles, that are not included in an uncertainty model (as they are not directly related

25   to pure instrument performance) but that are significant and possibly even dominant over land.

To compare MAP retrievals with AERONET or HSRL-2, $\chi^2 < 1.5$ is used in this paper (for SPEX, RSP, and AirMSPI) as the filter for the goodness of fit. Besides, we also apply filters on the number of viewing angles (≥ 9), the smallest scattering angle ($< 120°$), and the largest scattering angle ($> 120°$). To evaluate the retrieved aerosol properties, three measures are used, which are the Mean Absolute Error (MAE), the bias, and the STandard Deviation (STD). Two types of plots are included in this paper

30   for comparisons. One is the scatter plot with x- and y-axis respectively for two instruments. The other one is the Bland-Altman

(Martin Bland and Altman, 1986) plot (difference plot), where the differences between two instruments are plotted against the
the averages of the two intruments.

4.1 SPEX airborne, RSP, and AirMSPI versus AERONET

We first compare the polarimetric (SPEX, RSP, and AirMSPI) retrievals with the AERONET data for the aerosol optical depth

5 (AOD) at three wavelengths 380 nm, 440 nm, and 675 nm. For the comparison, retrievals within 10 km around each AERONET
station are selected and averaged. The AERONET data are averaged within 1 hour around the time of the ER-2 overpass. The
results of the AOD comparison are shown in Figure 1 where panels a,d correspond to SPEX airborne, panels b,e to RSP,
and panels c,f to AirMSPI. The 12 overpasses between SPEX and AERONET are consistent with those between RSP and
AERONET, i.e., one averaged value from SPEX (Fig 1a) and RSP (Fig 1b) correspond to the same averaged value from

10 AERONET. For AirMSPI (Fig 1c), 8 overpasses are consistent with SPEX and RSP, while the other 4 comparison points do
not have corresponding points for SPEX and RSP. The reason for this inconsistency in comparison points is that AirMSPI was
not making measurements for some of the AERONET overpasses. On the other hand some of the SPEX and RSP overpasses
are screened out because there were no ground pixels with enough co-located viewing angles because of aircraft yaw, while
the swath of AirMSPI is sufficiently large to still get co-located angles despite the yaw.

15 For the AOD at 440 nm, the MAE is respectively 0.016, 0.024, 0.014, the bias is respectively 0.003, -0.010, -0.004, and the
STD is respectively 0.019, 0.027, 0.017 for SPEX, RSP, and AirMSPI. The MAE, bias, and STD agree within 0.01 between the
instruments, where the values for SPEX airborne and AirMSPI are somewhat smaller than for RSP. Similar conclusions hold
for the AOD at 380 nm or 675 nm. For each instrument, the MAE gets smaller with increasing wavelengths, which is mainly
caused by the fact that the AOD value itself decreases with wavelength. Based on the comparisons above, we can conclude

20 that the SPEX, RSP, and AirMSPI all achieve good agreement with AERONET and the differences in performance between
the instruments are small.

For the comparison of the fine and coarse mode effective radius ($r_{\mathrm{eff}}^{\mathrm{f}}$ and $r_{\mathrm{eff}}^{\mathrm{c}}$), it should be noted that it is difficult to retrieve
them when AOD is small. Therefore, shown in Figure 2 are the comparison when τ_{380} is larger than 0.1. The remaining cases
are still very challenging but we would lose too many points if we further increase the AOD limit. The solid lines shown in the

25 plot are bias±STD. The retrievals of $r_{\mathrm{eff}}^{\mathrm{f}}$ compared with AERONET are shown in Figs. 2a-c, where the MAE is 0.022, 0.021,
and 0.028 μm for SPEX, RSP, and AirMSPI, respectively. SPEX and RSP compare somewhat better in terms of MAE and bias
whereas AirMSPI has a small STD. However, overall the differences between the instruments are small and the number of
comparison points is very limited, which means that differences between instruments can be explained by 1 or 2 points. The
$r_{\mathrm{eff}}^{\mathrm{c}}$ comparisons corresponding to SPEX, RSP, and AirMSPI are shown in Figs 2d-f, respectively. All three instruments have

30 a poor comparison with AERONET for $r_{\mathrm{eff}}^{\mathrm{c}}$, with a MAE close to 1.5 μm. It is known from synthetic studies (e.g., Hasekamp
et al. (2019)) that $r_{\mathrm{eff}}^{\mathrm{c}}$ is a difficult parameter to retrieve, in particular for small AOD values. It should be noted that AERONET
consistently gives larger coarse mode effective radius than MAPs. A possible explanation is that the effective radius for the
coarse mode 4 and 5 in our 5-mode retrieval are 0.882 and 1.719 respectively (see Table 1), thus the coarse mode effective
radius from MAPs calculated based on Eq. (4) is estimated and limited between 0.882 and 1.719, wheras AERONET gives

values between 2.25 and 3.3 (when τ_{380} is larger than 0.1). A comparable range is expected for MAPs if a parametric 2-mode retrieval or a $\geq$ 7-mode retrieval (Fu and Hasekamp, 2018) is used.

For the comparison of the fine and coarse mode AOD (τ^{f} and τ^{c}), the results are shown in Figure 3. SPEX, RSP, and AirMSPI all agree well with AERONET for τ^{f} with an MAE of respectively 0.028, 0.029, 0.012 and bias of respectively 0.028, 0.019, -0.004. The coarse mode AOD (τ^{c}) for SPEX, RSP, and AirMSPI are compared with AERONET in Figs 3d-f. The MAE is respectively 0.026, 0.028, 0.017 and the bias is respectively -0.025, -0.028, 0.003. For both the fine and coarse mode AOD, both SPEX and RSP have comparable performance against AERONET while AirMSPI compares somewhat better. Again, it should be noted that the AirMSPI comparison does not contain exactly the same points as the comparison for SPEX and RSP.

4.2 Comparison between SPEX airborne, RSP, and HSRL-2

For the comparison to HSRL-2, we only use SPEX airborne and RSP because these provided a continuous data stream during ACEPOL, while AirMSPI only provides step-and-stare measurements for specific targets.

4.2.1 Comparison HSRL-2 to AERONET

Given that we use HSRL-2 as a reference for our MAP retrievals, it is important to first validate HSRL-2 with AERONET, in particular because for many cases the HSRL-2 AOD is computed assuming a fixed lidar ratio. Figure 4 shows the comparison of the HSRL-2 AOD at 355 nm and 532 nm with AERONET (log-log interpolated between 340 and 380 nm for 355 nm and between 500 and 675 nm for 532 nm). From this comparison it follows that the HSRL-2 AOD at 532 nm agrees very well with AERONET, with a small MAE (0.012), a small absolute bias (0.005), and a small STD (0.014). The comparison at 355 nm is somewhat worse than that at 532 nm with an MAE of 0.028, a bias of -0.014, and a STD of 0.029. Note that shown in Figure 4 are the AOD with the assumed lidar ratio, and the points are corresponding to days 23 October, 25 October, 27 October, and 7 November 2017.

4.2.2 Low AOD case on 26 October 2017

In this subsection, we compare the aerosol properties from SPEX and RSP with those from HSRL-2 for the day 26 October 2017 with low aerosol loading (AOD at 532 nm in the range 0.02 to 0.14). The results for AOD at 355 nm and 532 nm are shown in Figure 5. Figure 5a shows the retrieved AOD from HSRL-2 for the ground pixels co-located with SPEX and RSP. From this figure it follows that there were very low AOD values for the eastern part of the scene and somewhat higher values in the Central Valley and close to Los Angeles. Figure 5b shows the AOD comparison between SPEX and HSRL-2 with the MAE 0.014, the bias 0.009, and the STD 0.018 at 532 nm, and the MAE 0.028, the bias -0.006, and the STD 0.034 at 355 nm. Figure 5c shows the AOD comparison between RSP and HSRL-2 with the MAE 0.022, the bias -0.007, and the STD 0.028 at 532 nm, and the MAE 0.037, the bias -0.008, and the STD 0.048 at 355 nm. So, SPEX shows a very good agreement with HSRL-2 for this challenging scene of low AOD over land with a relatively bright surface. SPEX compares somewhat better to HSRL-2 than RSP for this case at both 532 and 355 nm. The Bland-Altman plots Figs 5e and f show a larger scatter and more

outliers for RSP. A possible explanation is that for low AOD the effect of the surface on the measured radiances (and hence also DoLP) is larger than for SPEX airborne. For these cases there is larger sensitivity to spatial mismatch between different viewing angles, and RSP, as a single-pixel-swath instrument, is more sensitive to such mismatches. Figure 5d shows the AOD comparison between SPEX and RSP with the MAE 0.024, the bias 0.016, and the STD 0.025. The differences from the direct

5 comparison between SPEX and RSP are somewhat larger than those from individual comparisons with HSRL-2 of SPEX and RSP, respectively. This suggests that the differences with HSRL-2 are not caused by common assumptions in the SPEX and RSP retrievals, but are rather caused by errors that are specific to each MAP.

4.2.3 High AOD on 9 November 2017

In this subsection, polarimetric retrievals from SPEX airborne and RSP are compared to HSRL-2 on the day 9 November 2017

10 for a smoke plume with high AOD (including AOD values > 1.0). Figure 6a shows the HSRL-2 AOD at 355 nm and 532 nm for the flight leg over the smoke plume. Figure 6b shows the AOD comparison between SPEX and HSRL-2, where the MAE is 0.088, the bias is -0.029, and the STD is 0.149 at 532 nm. Figure 6c shows the AOD comparison between RSP and HSRL-2, where the MAE is 0.079, the bias is -0.024, and the STD is 0.142 at 532 nm. Figure 6d shows the AOD comparison between SPEX and RSP, where the MAE is 0.044, the bias is -0.005, and the STD is 0.063 at 532 nm. RSP compares slightly better

15 to HSRL-2 than SPEX with respect to MAE. It should be noted that the smoke plume exhibits large spatial variation so part of the MAP-lidar differences can be attributed to the fact that different instruments see a slightly different part of the smoke plume. Furthermore, both SPEX and RSP show a similar negative bias in AOD at both 355 nm and 532 nm, and one clear outlier point in the comparison with HSRL-2 at the highest AOD. This is also clear from the corresponding Bland-Altman plots Figs 6e and f. Given the very similar underestimation in both SPEX and RSP (compared to HSRL-2) and the good

20 comparison between SPEX and RSP, it is unlikely that this underestimation is caused by aspects related to instrumental errors of the 2 different MAPs. It might be possible that the underestimation is related to the MAP retrieval approach which is the same for both instruments, but based on earlier studies with real and synthetic measurements we have no indication for this. Another possibility is that HSRL-2 overestimates the AOD at this high aerosol loading or the large spatial variability has a larger effect on the MAP-lidar comparison than on the inter-MAP comparison. At high AOD the performance of RSP is more

25 similar to that of SPEX than for low AOD. Our explanation for this, is that at high AOD the measured radiance and DoLP are less affected by the co-registration errors between viewing angles than for low AOD.

For the high AOD case, we compare also the aerosol depolarization ratio (δ) and aerosol lidar ratio (S) from SPEX and RSP with HSRL-2. Figs 7a-c respectively show the comparison of the aerosol depolarization ratio between SPEX and HSRL-2, between RSP and HSRL-2, and between SPEX and RSP. It can be observed that both SPEX and RSP show a similar behavior

30 against HSRL-2 especially at 355 nm: There is an underestimation towards lower values of depolarization ratio but on the other hand there is a reasonable agreement with HSRL-2 for both instruments. Again, given the fact that the performance of both SPEX and RSP versus HSRL-2 is very similar, we conclude that the main reason for difference between SPEX/RSP and HSRL-2 does not lie in instrumental errors for the MAPs. A possible explanation for the difference could be the simplified description of non-spherical particles in our retrieval approach. On the other hand, the overall comparison of the aerosol depolarization

ratio with HSRL-2 confirms capability of both SPEX and RSP to retrieve information on particle shape. The results of the aerosol lidar ratio are shown in Figs 7d-f. Both SPEX and RSP show a similar overestimation of the lidar ratio compared to HSRL-2, and SPEX and RSP agree quite well. Again, it is unlikely that the overestimation is related to instrumental errors in the MAPs. Overall, the agreement with HSRL-2 for the aerosol lidar ratio is reasonable for both SPEX and RSP.

5 ### 4.2.4   Mean properties of the smoke plume for other aerosol properties

The mean aerosol properties for the smoke plume as measured by SPEX and RSP are summarized in Table 2. Here, we only include retrievals for which AOD > 0.2 at 532 nm because for those cases accurate retrieval of microphysical properties is expected (e.g., Hasekamp et al. (2019)). The number of points to calculate the mean properties is the same for SPEX and RSP. Also, we only include fine mode microphysical properties because there is only a very small coarse mode contribution to the

10 smoke plume. SPEX and RSP compare well for the fine mode refractive index, fine mode effective redius, fine and coarse mode AOD, and SSA (relative to requirements as formulated e.g. by Mishchenko et al. (2004)). Reasonable agreement is found for the fraction of spherical particles. For the Aerosol Layer Height (ALH), SPEX retrieves a much higher value than RSP, where the latter value is closer to the ALH derived from HSRL-2 (2.64 km). Here, it should be noted that for SPEX the shortest wavelength that is used in the retrieval is 450 nm, so we do not expect an accurate ALH retrieval (Wu et al., 2016).

15 The values of the aerosol properties in Table 2 (for both SPEX and RSP) are in the range that is expected for smoke. First of all, it is expected that smoke is dominated by fine particles (e.g. Russell et al. (2014)), which is confirmed by the much larger retrieved fine mode AOD than coarse mode AOD by both MAPs. The real part of the refractive index is consistent with the study of Levin et al. (2010) for the Fire Laboratory at Missoula Experiment (FLAME), who found mostly refractive indices for biomass burning between 1.55 and 1.60. Also, the SSA values in Table 2 are representative for fresh biomass burning smoke.

20 For example, Nicolae et al. (2013) found SSA values of 0.79 at 532 nm for smoke with an age of 0.25 day and 0.93 for smokes with an age of 0.75 day. Both the values retrieved by SPEX and RSP can be considered realistic for smoke.

5   Discussions and conclusions

In this study, we performed aerosol retrievals from different MAPs employed during the ACEPOL campaign and evaluated them against ground based AERONET measurements and against HSRL-2 measurements. The polarimetric aerosol retrievals

25 were performed using the SRON algorithm in multi-mode setup (Fu and Hasekamp, 2018) on SPEX airborne, RSP (without SWIR channels), and AirMSPI.

For the AERONET comparison, only scenes with low AOD (0.03-0.17 at 440 nm) were available during ACEPOL. For these scenes, SPEX, RSP, and AirMSPI all show good agreement with AERONET for AOD (MAE respectively 0.016, 0.024, and 0.014 for AOD at 440 nm). For the fine mode effective radius, we found MAE with AERONET of 0.022, 0.021, and 0.028

30 for SPEX, RSP, and AirMSPI, respectively. For the effective radius comparison we only compare scenes with AOD > 0.10 at 380 nm, but it should be noted that the remaining cases are still very challenging and that the difference in performance between the different instruments are caused by just 1 or 2 comparison points. All three instruments had a poor comparison

with AERONET for the coarse mode effective radius. This was because the coarse mode effective radius was a difficult parameter to retrieve, in particular for small AOD values. For the fine mode AOD, good agreements with AERONET were shown for all three MAPs with somewhat better performance for AirMSPI. For the coarse mode AOD, SPEX and RSP show reasonable agreement while AirMSPI shows also good agreement here. It should be noted however that the comparison for

5 AirMSPI is not based on exactly the same points as for SPEX and RSP.

For the comparison between the MAPs (SPEX and RSP) and HSRL-2, we focused on a day with low AOD and a flight leg with high AOD (including measurements with AOD > 1.0) over a prescribed forest fire in Arizona (9 November). For the challenging case of low AOD over land, it was shown that SPEX and RSP are capable of providing accurate retrievals of AOD. For this low AOD case, SPEX showed better comparison against HSRL-2 than RSP.

10 For the retrievals over the smoke plume also a reasonable agreement in AOD between the MAPs and HSRL-2 was found, despite the fact that the comparison was hampered by large spatial variability in AOD throughout the smoke plume. Besides, a good agreement was found between the MAPs (SPEX, RSP) and HSRL-2 for the aerosol depolarization ratio, which indicates MAPs are capable of retrieving particles sphericity. A reasonable comparison was also found for the aerosol lidar ratio.

For the ALH SPEX retrieves a value that is too high (by ∼1.5 km) compared to HSRL-2 while the ALH retrieved from RSP

15 agrees somewhat better with HSRL-2, although it is ∼1 km lower. Here, it should be noted that we do not expect a good ALH retrieval from SPEX airborne, because the shortest wavelength used in the retrieval was 450 nm. For the retrieved microphysical and optical properties of the smoke plume, SPEX and RSP agree very well with each other and both instruments retrieve smoke properties that are in line with earlier studies.

Data availability. The ACEPOL data from MAPs and lidars can be downloaded from the website: https://www-air.larc.nasa.gov/cgi-bin/

20 ArcView/acepol, (registration required). The AERONET data can be downloaded from the website: https://aeronet.gsfc.nasa.gov/. The meteorological NCEP data can be accessed through the website: http://www.cdc.noaa.gov/. The polarimetric retrieval results will be made available on SRON's ftp site.

Competing interests. The authors declare that no competing interests are present.

Acknowledgements. This work is funded by a NWO/NSO project ACEPOL: Aerosol Characterization from Polarimeter and Lidar under

25 project number ALW-GO/16-09. We thank NASA for the flight funding. We thank all the members involved in the ACEPOL campaign. We thank the AERONET team and the MERRA-2 team for maintaining the data. NCEP Reanalysis data provided by the NOAA/OAR/ESRL PSD, Boulder, Colorado, USA, from their website at https://www.esrl.noaa.gov/psd/. We would also like to thank the Netherlands Supercomputing Centre (SURFsara) for providing us with the computing facility, the Cartesius cluster.

References

Bottiger, J. R., Fry, E. S., and Thompson, R. C.: Phase Matrix Measurements for Electromagnetic Scattering by Sphere Aggregates, in: Light Scattering by Irregularly Shaped Particles, edited by Schuerman, D. W., pp. 283–290, Springer US, Boston, MA, https://doi.org/10.1007/978-1-4684-3704-1_33, 1980.

5 Burton, S. P., Ferrare, R. A., Hostetler, C. A., Hair, J. W., Rogers, R. R., Obland, M. D., Butler, C. F., Cook, A. L., Harper, D. B., and Froyd, K. D.: Aerosol classification using airborne High Spectral Resolution Lidar measurements – methodology and examples, Atmospheric Measurement Techniques, 5, 73–98, https://www.atmos-meas-tech.net/5/73/2012/, 2012.

Burton, S. P., Vaughan, M. A., Ferrare, R. A., and Hostetler, C. A.: Separating mixtures of aerosol types in airborne High Spectral Resolution Lidar data, Atmospheric Measurement Techniques, 7, 419–436, https://www.atmos-meas-tech.net/7/419/2014/amt-7-419-2014.html, 10 2014.

Burton, S. P., Hair, J. W., Kahnert, M., Ferrare, R. A., Hostetler, C. A., Cook, A. L., Harper, D. B., Berkoff, T. A., Seaman, S. T., Collins, J. E., Fenn, M. A., and Rogers, R. R.: Observations of the spectral dependence of linear particle depolarization ratio of aerosols using NASA Langley airborne High Spectral Resolution Lidar, Atmospheric Chemistry and Physics, 15, 13 453–13 473, https://www.atmos-chem-phys.net/15/13453/2015/, 2015.

15 Burton, S. P., Hostetler, C. A., Cook, A. L., Hair, J. W., Seaman, S. T., Scola, S., Harper, D. B., Smith, J. A., Fenn, M. A., Ferrare, R. A., Saide, P. E., Chemyakin, E. V., and Müller, D.: Calibration of a high spectral resolution lidar using a Michelson interferometer, with data examples from ORACLES, Applied Optics, 57, 6061–6075, https://www.osapublishing.org/ao/abstract.cfm?uri=ao-57-21-6061, 2018.

Cairns, B., Russell, E. E., and Travis, L. D.: Research Scanning Polarimeter: calibration and ground-based measurements, in: Polarization: Measurement, Analysis, and Remote Sensing II, vol. 3754, pp. 186–197, International Society for Op- 20 tics and Photonics, https://doi.org/10.1117/12.366329, https://www.spiedigitallibrary.org/conference-proceedings-of-spie/3754/0000/Research-Scanning-Polarimeter-calibration-and-ground-based-measurements/10.1117/12.366329.short, 1999.

Cairns, B., Russell, E. E., LaVeigne, J. D., and Tennant, P. M. W.: Research scanning polarimeter and airborne us-age for remote sensing of aerosols, in: Polarization Science and Remote Sensing, vol. 5158, pp. 33–44, Interna-tional Society for Optics and Photonics, https://www.spiedigitallibrary.org/conference-proceedings-of-spie/5158/0000/ 25 Research-scanning-polarimeter-and-airborne-usage-for-remote-sensing-of/10.1117/12.518320.short, 2003.

Cairns, B., LaVeigne, J. D., Rael, A., and Granneman, R. D.: Atmospheric correction of HyperSpecTIR measurements using the research scanning polarimeter, in: Polarization: Measurement, Analysis, and Remote Sensing VI, 12 Apr. 2004, Orlando, Fla., vol. 5432 of *Proc. SPIE*, p. 95, https://doi.org/10.1117/12.542194, 2004.

Chen, C., Dubovik, O., Henze, D. K., Lapyonak, T., Chin, M., Ducos, F., Litvinov, P., Huang, X., and Li, L.: Retrieval of desert dust 30 and carbonaceous aerosol emissions over Africa from POLDER/PARASOL products generated by the GRASP algorithm, Atmospheric Chemistry and Physics, 18, 12 551–12 580, https://www.atmos-chem-phys.net/18/12551/2018/acp-18-12551-2018.html, 2018.

Chowdhary, J., Cairns, B., Mishchenko, M. I., Hobbs, P. V., Cota, G. F., Redemann, J., Rutledge, K., Holben, B. N., and Russell, E.: Retrieval of Aerosol Scattering and Absorption Properties from Photopolarimetric Observations over the Ocean during the CLAMS Experiment, Journal of the Atmospheric Sciences, 62, 1093–1117, https://doi.org/10.1175/JAS3389.1, 2005.

35 D'Almeida, G. A., Koepke, P., and Shettle, E. P.: Atmospheric Aerosols: Global Climatology and Radiative Characteristics, A Deepak Pub, Hampton, 1991.

Deschamps, P., Breon, F., Leroy, M., Podaire, A., Bricaud, A., Buriez, J., and Seze, G.: The POLDER mission: instrument characteristics and scientific objectives, IEEE Transactions on Geoscience and Remote Sensing, 32, 598–615, https://doi.org/10.1109/36.297978, 1994.

Deuzé, J. L., Goloub, P., Herman, M., Marchand, A., Perry, G., Susana, S., and Tanré, D.: Estimate of the aerosol properties over the ocean with POLDER, Journal of Geophysical Research: Atmospheres, 105, 15 329–15 346, https://agupubs.onlinelibrary.wiley.com/doi/abs/10.1029/2000JD900148, 2000.

Deuzé, J. L., Bréon, F. M., Devaux, C., Goloub, P., Herman, M., Lafrance, B., Maignan, F., Marchand, A., Nadal, F., Perry, G., and Tanré, D.: Remote sensing of aerosols over land surfaces from POLDER-ADEOS-1 polarized measurements, Journal of Geophysical Research: Atmospheres, 106, 4913–4926, https://agupubs.onlinelibrary.wiley.com/doi/abs/10.1029/2000JD900364, 2001.

Di Noia, A., Hasekamp, O. P., van Harten, G., Rietjens, J. H. H., Smit, J. M., Snik, F., Henzing, J. S., de Boer, J., Keller, C. U., and Volten, H.: Use of neural networks in ground-based aerosol retrievals from multi-angle spectropolarimetric observations, Atmospheric Measurement Techniques, 8, 281–299, https://www.atmos-meas-tech.net/8/281/2015/, 2015.

Di Noia, A., Hasekamp, O. P., Wu, L., van Diedenhoven, B., Cairns, B., and Yorks, J. E.: Combined neural network/Phillips-Tikhonov approach to aerosol retrievals over land from the NASA Research Scanning Polarimeter, Atmospheric Measurement Techniques, 10, 4235–4252, https://doi.org/10.5194/amt-10-4235-2017, 2017.

Diner, D. J., Xu, F., Garay, M. J., Martonchik, J. V., Rheingans, B. E., Geier, S., Davis, A., Hancock, B. R., Jovanovic, V. M., Bull, M. A., Capraro, K., Chipman, R. A., and McClain, S. C.: The Airborne Multiangle SpectroPolarimetric Imager (AirMSPI): a new tool for aerosol and cloud remote sensing, Atmospheric Measurement Techniques, 6, 2007–2025, https://doi.org/10.5194/amt-6-2007-2013, 2013.

Diner, D. J., Boland, S. W., Brauer, M., Bruegge, C., Burke, K. A., Chipman, R., Girolamo, L. D., Garay, M. J., Hasheminassab, S., Hyer, E., Jerrett, M., Jovanovic, V., Kalashnikova, O. V., Liu, Y., Lyapustin, A. I., Martin, R. V., Nastan, A., Ostro, B. D., Ritz, B., Schwartz, J., Wang, J., and Xu, F.: Advances in multiangle satellite remote sensing of speciated airborne particulate matter and association with adverse health effects: from MISR to MAIA, Journal of Applied Remote Sensing, 12, 042 603, https://www.spiedigitallibrary.org/journals/Journal-of-Applied-Remote-Sensing/volume-12/issue-4/042603/Advances-in-multiangle-satellite-remote-sensing-of-speciated-airborne-particulate/10.1117/1.JRS.12.042603.short, 2018.

Dubovik, O., Holben, B. N., Lapyonok, T., Sinyuk, A., Mishchenko, M. I., Yang, P., and Slutsker, I.: Non-spherical aerosol retrieval method employing light scattering by spheroids, Geophys. Res. Lett., 29, 1415+, https://doi.org/10.1029/2001gl014506, 2002.

Dubovik, O., Sinyuk, A., Lapyonok, T., Holben, B. N., Mishchenko, M., Yang, P., Eck, T. F., Volten, H., Muñoz, O., Veihelmann, B., van der Zande, W. J., Leon, J. F., Sorokin, M., and Slutsker, I.: Application of spheroid models to account for aerosol particle nonsphericity in remote sensing of desert dust, Journal of Geophysical Research (Atmospheres), 111, D11 208+, https://doi.org/10.1029/2005jd006619, 2006.

Dubovik, O., Herman, M., Holdak, A., Lapyonok, T., Tanré, D., Deuzé, J. L., Ducos, F., Sinyuk, A., and Lopatin, A.: Statistically optimized inversion algorithm for enhanced retrieval of aerosol properties from spectral multi-angle polarimetric satellite observations, Atmospheric Measurement Techniques, 4, 975–1018, https://doi.org/10.5194/amt-4-975-2011, 2011.

Dubovik, O., Li, Z., Mishchenko, M. I., Tanré, D., Karol, Y., Bojkov, B., Cairns, B., Diner, D. J., Espinosa, W. R., Goloub, P., Gu, X., Hasekamp, O., Hong, J., Hou, W., Knobelspiesse, K. D., Landgraf, J., Li, L., Litvinov, P., Liu, Y., Lopatin, A., Marbach, T., Maring, H., Martins, V., Meijer, Y., Milinevsky, G., Mukai, S., Parol, F., Qiao, Y., Remer, L., Rietjens, J., Sano, I., Stammes, P., Stamnes, S., Sun, X., Tabary, P., Travis, L. D., Waquet, F., Xu, F., Yan, C., and Yin, D.: Polarimetric remote sensing of atmospheric aerosols: Instruments, methodologies, results, and perspectives, Journal of Quantitative Spectroscopy and Radiative Transfer, 224, 474–511, http://www.sciencedirect.com/science/article/pii/S0022407318308409, 2019.

Fougnie, B., Marbach, T., Lacan, A., Lang, R., Schlüssel, P., Poli, G., Munro, R., and Couto, A. B.: The multi-viewing multi-channel multi-polarisation imager – Overview of the 3MI polarimetric mission for aerosol and cloud characterization, Journal of Quantitative Spectroscopy and Radiative Transfer, 219, 23–32, http://www.sciencedirect.com/science/article/pii/S002240731830373X, 2018.

Fu, G. and Hasekamp, O.: Retrieval of aerosol microphysical and optical properties over land using a multimode approach, Atmospheric Measurement Techniques, 11, 6627–6650, https://doi.org/10.5194/amt-11-6627-2018, 2018.

Gao, M., Zhai, P.-W., Franz, B., Hu, Y., Knobelspiesse, K., Werdell, P. J., Ibrahim, A., Cairns, B., and Chase, A.: Inversion of multi-angular polarimetric measurements over open and coastal ocean waters: a joint retrieval algorithm for aerosol and water leaving radiance properties, Atmospheric Measurement Techniques Discussions, pp. 1–31, https://www.atmos-meas-tech-discuss.net/amt-2019-67/, 2019.

Gelaro, R., McCarty, W., Suárez, M. J., Todling, R., Molod, A., Takacs, L., Randles, C. A., Darmenov, A., Bosilovich, M. G., Reichle, R., Wargan, K., Coy, L., Cullather, R., Draper, C., Akella, S., Buchard, V., Conaty, A., da Silva, A. M., Gu, W., Kim, G.-K., Koster, R., Lucchesi, R., Merkova, D., Nielsen, J. E., Partyka, G., Pawson, S., Putman, W., Rienecker, M., Schubert, S. D., Sienkiewicz, M., and Zhao, B.: The Modern-Era Retrospective Analysis for Research and Applications, Version 2 (MERRA-2), Journal of Climate, 30, 5419–5454, https://journals.ametsoc.org/doi/full/10.1175/JCLI-D-16-0758.1, 2017.

Hair, J. W., Hostetler, C. A., Cook, A. L., Harper, D. B., Ferrare, R. A., Mack, T. L., Welch, W., Izquierdo, L. R., and Hovis, F. E.: Airborne High Spectral Resolution Lidar for profiling aerosol optical properties, Appl. Opt., 47, 6734–6752, http://ao.osa.org/abstract.cfm?URI=ao-47-36-6734, 2008.

Hansen, J. E. and Travis, L. D.: Light scattering in planetary atmospheres, Space Science Reviews, 16, 527–610, https://doi.org/10.1007/BF00168069, https://doi.org/10.1007/BF00168069, 1974.

Hasekamp, O. P.: Capability of multi-viewing-angle photo-polarimetric measurements for the simultaneous retrieval of aerosol and cloud properties, Atmospheric Measurement Techniques, 3, 839–851, https://doi.org/10.5194/amt-3-839-2010, 2010.

Hasekamp, O. P. and Landgraf, J.: A linearized vector radiative transfer model for atmospheric trace gas retrieval, J. Quant. Spec. Radiat. Transf., 75, 221–238, https://doi.org/10.1016/s0022-4073(01)00247-3, 2002.

Hasekamp, O. P. and Landgraf, J.: Retrieval of aerosol properties over the ocean from multispectral single-viewing-angle measurements of intensity and polarization: Retrieval approach, information content, and sensitivity study, J. Geophys. Res., 110, D20 207+, https://doi.org/10.1029/2005jd006212, 2005.

Hasekamp, O. P. and Landgraf, J.: Retrieval of aerosol properties over land surfaces: capabilities of multiple-viewing-angle intensity and polarization measurements, Appl. Opt., 46, 3332–3344, https://doi.org/10.1364/ao.46.003332, 2007.

Hasekamp, O. P., Litvinov, P., and Butz, A.: Aerosol properties over the ocean from PARASOL multiangle photopolarimetric measurements, J. Geophys. Res., 116, D14 204+, https://doi.org/10.1029/2010jd015469, 2011.

Hasekamp, O. P., Fu, G., Rusli, S. P., Wu, L., Di Noia, A., Brugh, J. a. d., Landgraf, J., Martijn Smit, J., Rietjens, J., and van Amerongen, A.: Aerosol measurements by SPEXone on the NASA PACE mission: expected retrieval capabilities, Journal of Quantitative Spectroscopy and Radiative Transfer, 227, 170–184, http://www.sciencedirect.com/science/article/pii/S0022407318308653, 2019.

Hill, S. C., Hill, A. C., and Barber, P. W.: Light scattering by size/shape distributions of soil particles and spheroids, Appl. Opt., 23, 1025–1031, https://doi.org/10.1364/ao.23.001025, 1984.

Holben, B. N., Tanré, D., Smirnov, A., Eck, T. F., Slutsker, I., Abuhassan, N., Newcomb, W. W., Schafer, J. S., Chatenet, B., Lavenu, F., Kaufman, Y. J., Castle, J. V., Setzer, A., Markham, B., Clark, D., Frouin, R., Halthore, R., Karneli, A., O'Neill, N. T., Pietras, C., Pinker, R. T., Voss, K., and Zibordi, G.: An emerging ground-based aerosol climatology: Aerosol optical depth from AERONET, J. Geophys. Res., 106, 12–12 097, https://doi.org/10.1029/2001jd900014, 2001.

Illingworth, A. J., Barker, H. W., Beljaars, A., Ceccaldi, M., Chepfer, H., Clerbaux, N., Cole, J., Delanoë, J., Domenech, C., Donovan, D. P., Fukuda, S., Hirakata, M., Hogan, R. J., Huenerbein, A., Kollias, P., Kubota, T., Nakajima, T., Nakajima, T. Y., Nishizawa, T., Ohno, Y., Okamoto, H., Oki, R., Sato, K., Satoh, M., Shephard, M. W., Velázquez-Blázquez, A., Wandinger, U., Wehr, T., and van Zadelhoff, G.-J.: The EarthCARE Satellite: The Next Step Forward in Global Measurements of Clouds, Aerosols, Precipitation, and Radiation, Bulletin of the American Meteorological Society, 96, 1311–1332, https://journals.ametsoc.org/doi/10.1175/BAMS-D-12-00227.1, 2014.

IPCC: IPCC, 2014: Climate Change 2014: Synthesis Report. Contribution of Working Groups I, II and III to the Fifth Assessment Report of the Intergovernmental Panel on Climate Change [Core Writing Team, R.K. Pachauri and L.A. Meyer (eds.)], Tech. rep., Geneva, Switzerland, https://www.ipcc.ch/report/ar5/syr/, 2014.

Kalnay, E., Kanamitsu, M., Kistler, R., Collins, W., Deaven, D., Gandin, L., Iredell, M., Saha, S., White, G., Woollen, J., Zhu, Y., Leetmaa, A., Reynolds, B., Chelliah, M., Ebisuzaki, W., Higgins, W., Janowiak, J., Mo, K. C., Ropelewski, C., Wang, J., Jenne, R., and Joseph, D.: The NCEP/NCAR 40-Year Reanalysis Project., Bulletin of the American Meteorological Society, 77, 437–472, https://doi.org/10.1175/1520-0477(1996)077%3C0437:tnyrp%3E2.0.co;2, 1996.

Knobelspiesse, K., Cairns, B., Mishchenko, M., Chowdhary, J., Tsigaridis, K., van Diedenhoven, B., Martin, W., Ottaviani, M., and Alexandrov, M.: Analysis of fine-mode aerosol retrieval capabilities by different passive remote sensing instrument designs., Optics express, 20, 21 457–21 484, 2012.

Knobelspiesse, K., Tan, Q., Bruegge, C., Cairns, B., Chowdhary, J., Diedenhoven, B. v., Diner, D., Ferrare, R., Harten, G. v., Jovanovic, V., Ottaviani, M., Redemann, J., Seidel, F., and Sinclair, K.: Intercomparison of airborne multi-angle polarimeter observations from the Polarimeter Definition Experiment, Applied Optics, 58, 650–669, https://www.osapublishing.org/ao/abstract.cfm?uri=ao-58-3-650, 2019.

Lacagnina, C., Hasekamp, O. P., Bian, H., Curci, G., Myhre, G., van Noije, T., Schulz, M., Skeie, R. B., Takemura, T., and Zhang, K.: Aerosol single-scattering albedo over the global oceans: Comparing PARASOL retrievals with AERONET, OMI, and AeroCom models estimates, Journal of Geophysical Research (Atmospheres), 120, 9814–9836, https://doi.org/10.1002/2015jd023501, 2015.

Lacagnina, C., Hasekamp, O. P., and Torres, O.: Direct radiative effect of aerosols based on PARASOL and OMI satellite observations, Journal of Geophysical Research (Atmospheres), 122, 2366–2388, https://doi.org/10.1002/2016jd025706, 2017.

Levin, E. J. T., McMeeking, G. R., Carrico, C. M., Mack, L. E., Kreidenweis, S. M., Wold, C. E., Moosmüller, H., Arnott, W. P., Hao, W. M., Collett, J. L., and Malm, W. C.: Biomass burning smoke aerosol properties measured during Fire Laboratory at Missoula Experiments (FLAME), Journal of Geophysical Research: Atmospheres, 115, https://agupubs.onlinelibrary.wiley.com/doi/abs/10.1029/2009JD013601, 2010.

Litvinov, P., Hasekamp, O., and Cairns, B.: Models for surface reflection of radiance and polarized radiance: Comparison with airborne multi-angle photopolarimetric measurements and implications for modeling top-of-atmosphere measurements, Remote Sensing of Environment, 115, 781–792, https://doi.org/https://doi.org/10.1016/j.rse.2010.11.005, 2011.

Lopes, F. J. S., Landulfo, E., and Vaughan, M. A.: Evaluating CALIPSO's 532 nm lidar ratio selection algorithm using AERONET sun photometers in Brazil, Atmospheric Measurement Techniques, 6, 3281–3299, https://www.atmos-meas-tech.net/6/3281/2013/, 2013.

Maignan, F., Bréon, F.-M., Fédèle, E., and Bouvier, M.: Polarized reflectances of natural surfaces: Spaceborne measurements and analytical modeling, Remote Sensing of Environment, 113, 2642–2650, https://doi.org/https://doi.org/10.1016/j.rse.2009.07.022, 2009.

Martin Bland, J. and Altman, D.: STATISTICAL METHODS FOR ASSESSING AGREEMENT BETWEEN TWO METHODS OF CLINICAL MEASUREMENT, The Lancet, 327, 307–310, http://www.sciencedirect.com/science/article/pii/S0140673686908378, 1986.

Martins, J. V., Fernandez-Borda, R., McBride, B., Remer, L., and Barbosa, H. M. J.: The Harp Hyperangular Imaging Polarimeter and the Need for Small Satellite Payloads with High Science Payoff for Earth Science Remote Sensing, in: IGARSS 2018 - 2018 IEEE International Geoscience and Remote Sensing Symposium, pp. 6304–6307, https://doi.org/10.1109/IGARSS.2018.8518823, 2018.

McGill, M., Hlavka, D., Hart, W., Scott, V. S., Spinhirne, J., and Schmid, B.: Cloud Physics Lidar: instrument description and initial mea-
5 surement results, Appl. Opt., 41, 3725–3734, https://doi.org/10.1364/AO.41.003725, 2002.

Mishchenko, M. I.: Electromagnetic Scattering by Particles and Particle Groups, https://doi.org/10.1017/CBO9781139019064, 2014.

Mishchenko, M. I. and Travis, L. D.: Satellite retrieval of aerosol properties over the ocean using measurements of reflected sun-
light: Effect of instrumental errors and aerosol absorption, Journal of Geophysical Research: Atmospheres, 102, 13 543–13 553,
https://doi.org/10.1029/97JD01124, 1997.

10 Mishchenko, M. I., Travis, L. D., Kahn, R. A., and West, R. A.: Modeling phase functions for dust-like tropospheric aerosols using a shape
mixture of randomly oriented polydisperse spheroids, J. Geophys. Res., 102, 13 543–13 553, https://doi.org/10.1029/97jd01124, 1997.

Mishchenko, M. I., Cairns, B., Hansen, J. E., Travis, L. D., Burg, R., Kaufman, Y. J., Martins, J. V., and Shettle, E. P.: Monitor-
ing of aerosol forcing of climate from space: analysis of measurement requirements, J. Quant. Spec. Radiat. Transf., 88, 149–161,
https://doi.org/10.1016/j.jqsrt.2004.03.030, 2004.

15 Mishchenko, M. I., Cairns, B., Kopp, G., Schueler, C. F., Fafaul, B. A., Hansen, J. E., Hooker, R. J., Itchkawich, T., Maring, H. B., and Travis,
L. D.: Accurate Monitoring of Terrestrial Aerosols and Total Solar Irradiance: Introducing the Glory Mission, Bulletin of the American
Meteorological Society, 88, 677–691, https://doi.org/10.1175/bams-88-5-677, 2007.

Mishchenko, M. I., Dlugach, J. M., and Liu, L.: Linear depolarization of lidar returns by aged smoke particles, Appl. Opt., 55, 9968+,
https://doi.org/10.1364/ao.55.009968, 2016.

20 Müller, D., Hostetler, C. A., Ferrare, R. A., Burton, S. P., Chemyakin, E., Kolgotin, A., Hair, J. W., Cook, A. L., Harper, D. B., Rogers,
R. R., Hare, R. W., Cleckner, C. S., Obland, M. D., Tomlinson, J., Berg, L. K., and Schmid, B.: Airborne Multiwavelength High Spectral
Resolution Lidar (HSRL-2) observations during TCAP 2012: vertical profiles of optical and microphysical properties of a smoke/urban
haze plume over the northeastern coast of the US, Atmospheric Measurement Techniques, 7, 3487–3496, https://www.atmos-meas-tech.
net/7/3487/2014/, 2014.

25 Navarro, R.: The NASA Earth Research-2 (ER-2) Aircraft: A Flying Laboratory for Earth Science Studies, Tech. rep., https://ntrs.nasa.gov/
search.jsp?R=20070014865, 2007.

Nicolae, D., Nemuc, A., Müller, D., Talianu, C., Vasilescu, J., Belegante, L., and Kolgotin, A.: Characterization of fresh and aged biomass
burning events using multiwavelength Raman lidar and mass spectrometry, Journal of Geophysical Research: Atmospheres, 118, 2956–
2965, https://agupubs.onlinelibrary.wiley.com/doi/abs/10.1002/jgrd.50324, 2013.

30 O'Neill, N. T., Eck, T. F., Smirnov, A., Holben, B. N., and Thulasiraman, S.: Spectral discrimination of coarse and fine mode optical depth,
Journal of Geophysical Research: Atmospheres, 108, https://agupubs.onlinelibrary.wiley.com/doi/abs/10.1029/2002JD002975, 2003.

Rahman, H., Pinty, B., and Verstraete, M. M.: Coupled surface-atmosphere reflectance (CSAR) model: 2. Semiempirical surface model
usable with NOAA advanced very high resolution radiometer data, Journal of Geophysical Research: Atmospheres, 98, 20 791–20 801,
https://doi.org/10.1029/93JD02072, https://agupubs.onlinelibrary.wiley.com/doi/abs/10.1029/93JD02072, 1993.

35 Rogers, R. R., Hair, J. W., Hostetler, C. A., Ferrare, R. A., Obland, M. D., Cook, A. L., Harper, D. B., Burton, S. P., Shinozuka, Y.,
McNaughton, C. S., Clarke, A. D., Redemann, J., Russell, P. B., Livingston, J. M., and Kleinman, L. I.: NASA LaRC airborne high
spectral resolution lidar aerosol measurements during MILAGRO: observations and validation, Atmospheric Chemistry and Physics, 9,
4811–4826, https://www.atmos-chem-phys.net/9/4811/2009/, 2009.

Russell, P. B., Kacenelenbogen, M., Livingston, J. M., Hasekamp, O. P., Burton, S. P., Schuster, G. L., Johnson, M. S., Knobelspiesse, K. D., Redemann, J., Ramachandran, S., and Holben, B.: A multiparameter aerosol classification method and its application to retrievals from spaceborne polarimetry, Journal of Geophysical Research: Atmospheres, 119, 9838–9863, https://agupubs.onlinelibrary.wiley.com/doi/abs/10.1002/2013JD021411, 2014.

5 Schepers, D., aan de Brugh, J. M. J., Hahne, P., Butz, A., Hasekamp, O. P., and Landgraf, J.: LINTRAN v2.0: A linearised vector radiative transfer model for efficient simulation of satellite-born nadir-viewing reflection measurements of cloudy atmospheres, Journal of Quantitative Spectroscopy and Radiative Transfer, 149, 347–359, http://www.sciencedirect.com/science/article/pii/S002240731400363X, 2014.

Smit, J. M., Rietjens, J. H. H., Harten, G. v., Noia, A. D., Laauwen, W., Rheingans, B. E., Diner, D. J., Cairns, B., Wasilewski, A., Kno-
10 belspiesse, K. D., Ferrare, R., and Hasekamp, O. P.: SPEX airborne spectropolarimeter calibration and performance, Applied Optics, 58, 5695–5719, https://www.osapublishing.org/ao/abstract.cfm?uri=ao-58-21-5695, 2019.

Snik, F., Karalidi, T., and Keller, C. U.: Spectral modulation for full linear polarimetry, Appl. Opt., 48, 1337–1346, https://doi.org/10.1364/AO.48.001337, 2009.

Stamnes, S., Hostetler, C., Ferrare, R., Burton, S., Liu, X., Hair, J., Hu, Y., Wasilewski, A., Martin, W., Diedenhoven, B. V., Chowdhary,
15 J., Cetinić, I., Berg, L. K., Stamnes, K., and Cairns, B.: Simultaneous polarimeter retrievals of microphysical aerosol and ocean color parameters from the "MAPP" algorithm with comparison to high-spectral-resolution lidar aerosol and ocean products, Appl. Opt., 57, https://doi.org/10.1364/ao.57.002394, 2018.

Stap, F. A., Hasekamp, O. P., and Röckmann, T.: Sensitivity of PARASOL multi-angle photopolarimetric aerosol retrievals to cloud contamination, Atmospheric Measurement Techniques, 8, 1287–1301, http://dx.doi.org/10.5194/amt-8-1287-2015, 2015.

20 Stap, F. A., Hasekamp, O. P., Emde, C., and Röckmann, T.: Multiangle photopolarimetric aerosol retrievals in the vicinity of clouds: Synthetic study based on a large eddy simulation, Journal of Geophysical Research: Atmospheres, 121, https://doi.org/10.1002/2016JD024787, 2016.

van Harten, G., de Boer, J., Rietjens, J. H. H., Di Noia, A., Snik, F., Volten, H., Smit, J. M., Hasekamp, O. P., Henzing, J. S., and Keller, C. U.: Atmospheric aerosol characterization with a ground-based SPEX spectropolarimetric instrument, Atmospheric Measurement Techniques,
25 7, 4341–4351, https://www.atmos-meas-tech.net/7/4341/2014/, 2014.

Waquet, F., Cairns, B., Knobelspiesse, K., Chowdhary, J., Travis, L. D., Schmid, B., and Mishchenko, M. I.: Polarimetric remote sensing of aerosols over land, Journal of Geophysical Research (Atmospheres), 114, D01 206+, https://doi.org/10.1029/2008jd010619, 2009.

Werdell, P. J., Behrenfeld, M. J., Bontempi, P. S., Boss, E., Cairns, B., Davis, G. T., Franz, B. A., Gliese, U. B., Gorman, E. T., Hasekamp, O., Knobelspiesse, K. D., Mannino, A., Martins, J. V., McClain, C. R., Meister, G., and Remer, L. A.: The Plankton, Aerosol, Cloud, ocean
30 Ecosystem (PACE) mission: Status, science, advances, Bulletin of the American Meteorological Society, https://journals.ametsoc.org/doi/abs/10.1175/BAMS-D-18-0056.1, 2019.

Winker, D. M., Pelon, J., Coakley, J. A., Ackerman, S. A., Charlson, R. J., Colarco, P. R., Flamant, P., Fu, Q., Hoff, R. M., Kittaka, C., Kubar, T. L., Le Treut, H., Mccormick, M. P., Mégie, G., Poole, L., Powell, K., Trepte, C., Vaughan, M. A., and Wielicki, B. A.: The CALIPSO Mission, Bulletin of the American Meteorological Society, 91, 1211–1230, https://doi.org/10.1175/2010BAMS3009.1, 2010.

35 Wu, L., Hasekamp, O., van Diedenhoven, B., and Cairns, B.: Aerosol retrieval from multiangle, multispectral photopolarimetric measurements: importance of spectral range and angular resolution, Atmospheric Measurement Techniques, 8, 2625–2638, https://doi.org/10.5194/amt-8-2625-2015, 2015.

Wu, L., Hasekamp, O., van Diedenhoven, B., Cairns, B., Yorks, J. E., and Chowdhary, J.: Passive remote sensing of aerosol layer height using near-UV multiangle polarization measurements, Geophys. Res. Lett., 43, 8783–8790, https://doi.org/10.1002/2016gl069848, 2016.

Wyzga, R. E. and Rohr, A. C.: Long-term particulate matter exposure: Attributing health effects to individual PM components, Journal of the Air & Waste Management Association, 65, 523–543, https://doi.org/10.1080/10962247.2015.1020396, 2015.

5   Xu, F., van Harten, G., Diner, D. J., Kalashnikova, O. V., Seidel, F. C., Bruegge, C. J., and Dubovik, O.: Coupled retrieval of aerosol properties and land surface reflection using the Airborne Multiangle SpectroPolarimetric Imager, Journal of Geophysical Research (Atmospheres), 122, 7004–7026, https://doi.org/10.1002/2017jd026776, 2017.

Xu, F., Harten, G. v., Diner, D. J., Davis, A. B., Seidel, F. C., Rheingans, B., Tosca, M., Alexandrov, M. D., Cairns, B., Ferrare, R. A., Burton, S. P., Fenn, M. A., Hostetler, C. A., Wood, R., and Redemann, J.: Coupled Retrieval of Liquid Water Cloud and Above-Cloud Aerosol

10   Properties Using the Airborne Multiangle SpectroPolarimetric Imager (AirMSPI), Journal of Geophysical Research: Atmospheres, 123, 3175–3204, https://agupubs.onlinelibrary.wiley.com/doi/abs/10.1002/2017JD027926, 2018.

Xu, F., Diner, D. J., Dubovik, O., and Schechner, Y.: A Correlated Multi-Pixel Inversion Approach for Aerosol Remote Sensing, Remote Sensing, 11, 746, https://www.mdpi.com/2072-4292/11/7/746, 2019.

Yorks, J. E., McGill, M. J., Scott, V. S., Wake, S. W., Kupchock, A., Hlavka, D. L., Hart, W. D., and Selmer, P. A.: The Airborne

15   Cloud–Aerosol Transport System: Overview and Description of the Instrument and Retrieval Algorithms, Journal of Atmospheric and Oceanic Technology, 31, 2482–2497, https://journals.ametsoc.org/doi/full/10.1175/JTECH-D-14-00044.1, 2014.
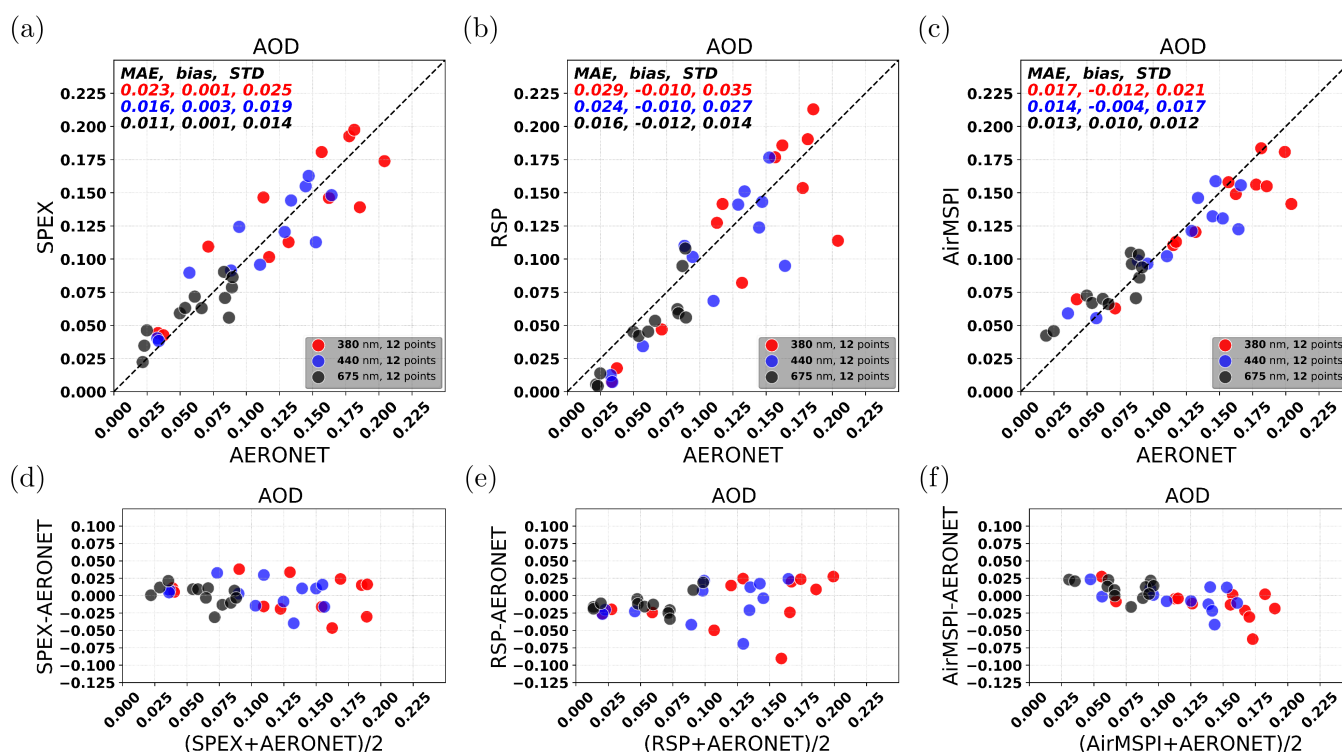
Figure 1. Comparison with AERONET for AOD (380 nm, 440 nm and 675 nm) among SPEX, RSP, and AirMSPI retrievals.
(a),**(b)**,**(c)** SPEX, RSP, and AirMSPI comparison with AERONET respectively. **(d)**,**(e)**,**(f)** Bland-Altman plots (or difference plots) between
SPEX and AERONET, between RSP and AERONET, and between AirMSPI and AERONET, respectively.
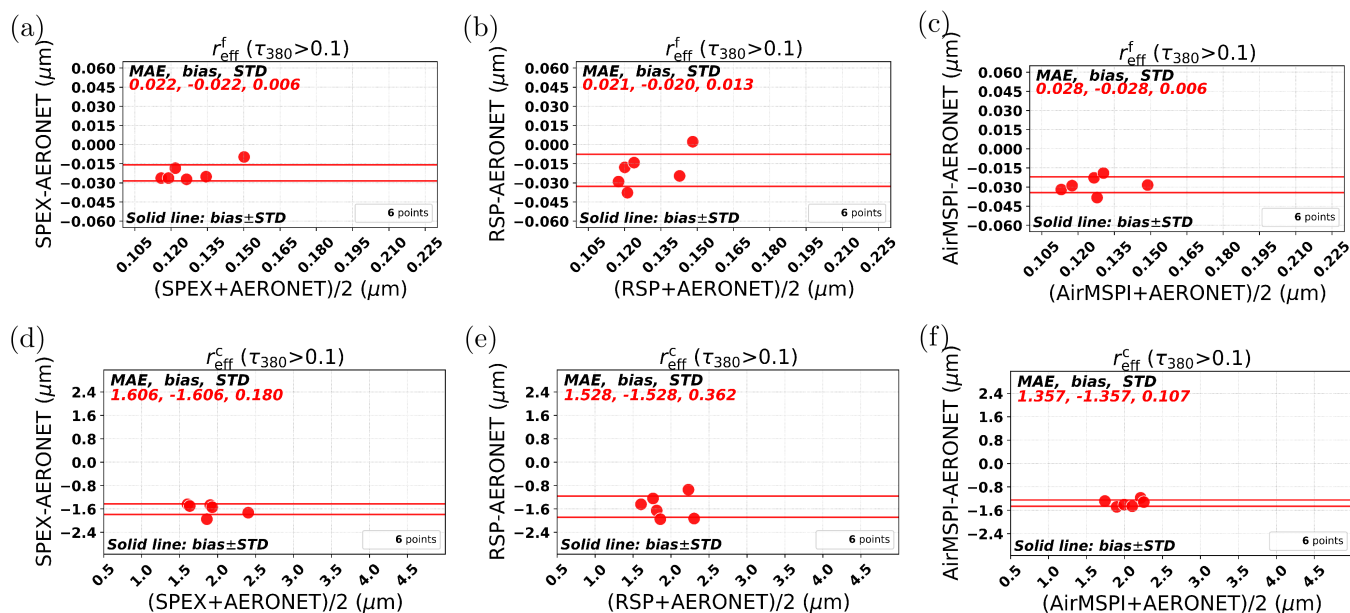
Figure 2. Comparison with AERONET for the effective radius of the fine and coarse modes ($r_{\mathrm{eff}}^{\mathrm{f}}$ and $r_{\mathrm{eff}}^{\mathrm{c}}$), among SPEX, RSP, and AirMSPI retrievals. (a),(b),(c) Bland-Altman plots for $r_{\mathrm{eff}}^{\mathrm{f}}$ between SPEX and AERONET, between RSP and AERONET, and between AirMSPI and AERONET, respectively. **(d),(e),(f)** Bland-Altman plots for $r_{\mathrm{eff}}^{\mathrm{c}}$ between SPEX and AERONET, between RSP and AERONET, and between AirMSPI and AERONET, respectively.
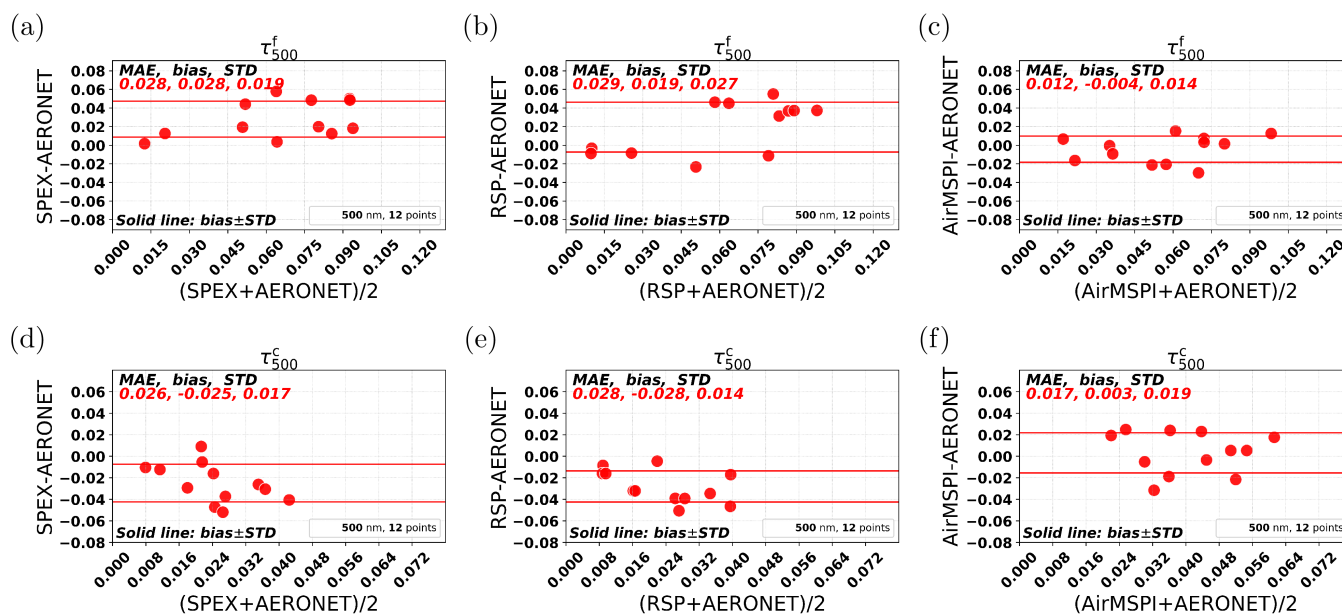
Figure 3. Comparison with AERONET for the AOD of the fine and coarse modes (τ^{f}_{500} **and** τ^{c}_{500}**) among SPEX, RSP, and AirMSPI retrievals. (a),(b),(c)** Bland-Altman plots for τ^{f}_{500} between SPEX and AERONET, between RSP and AERONET, and between AirMSPI and AERONET, respectively. **(d),(e),(f)** Bland-Altman plots for τ^{c}_{500} between SPEX and AERONET, between RSP and AERONET, and between AirMSPI and AERONET, respectively.
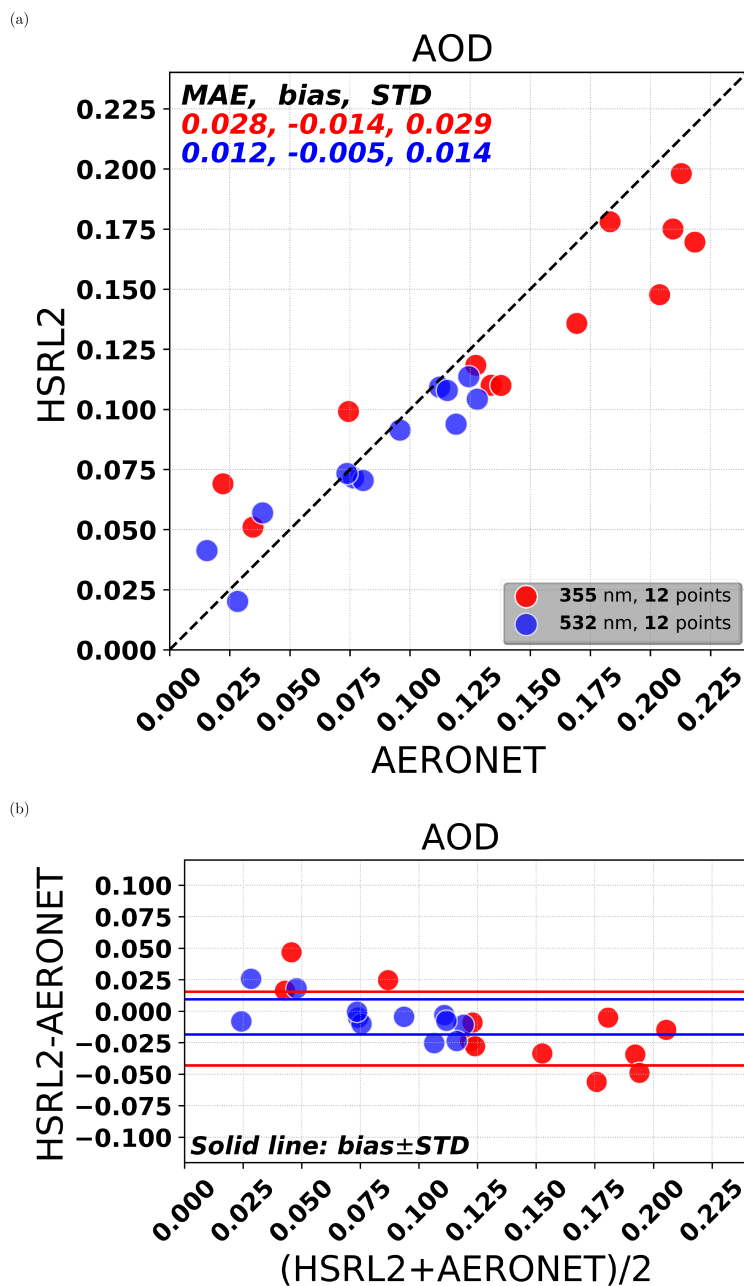
Figure 4. Comparison between HSRL-2 and AERONET for AOD at 355 nm and 532 nm. (a) and **(b)** are respectively the scatter plot and the difference plot.
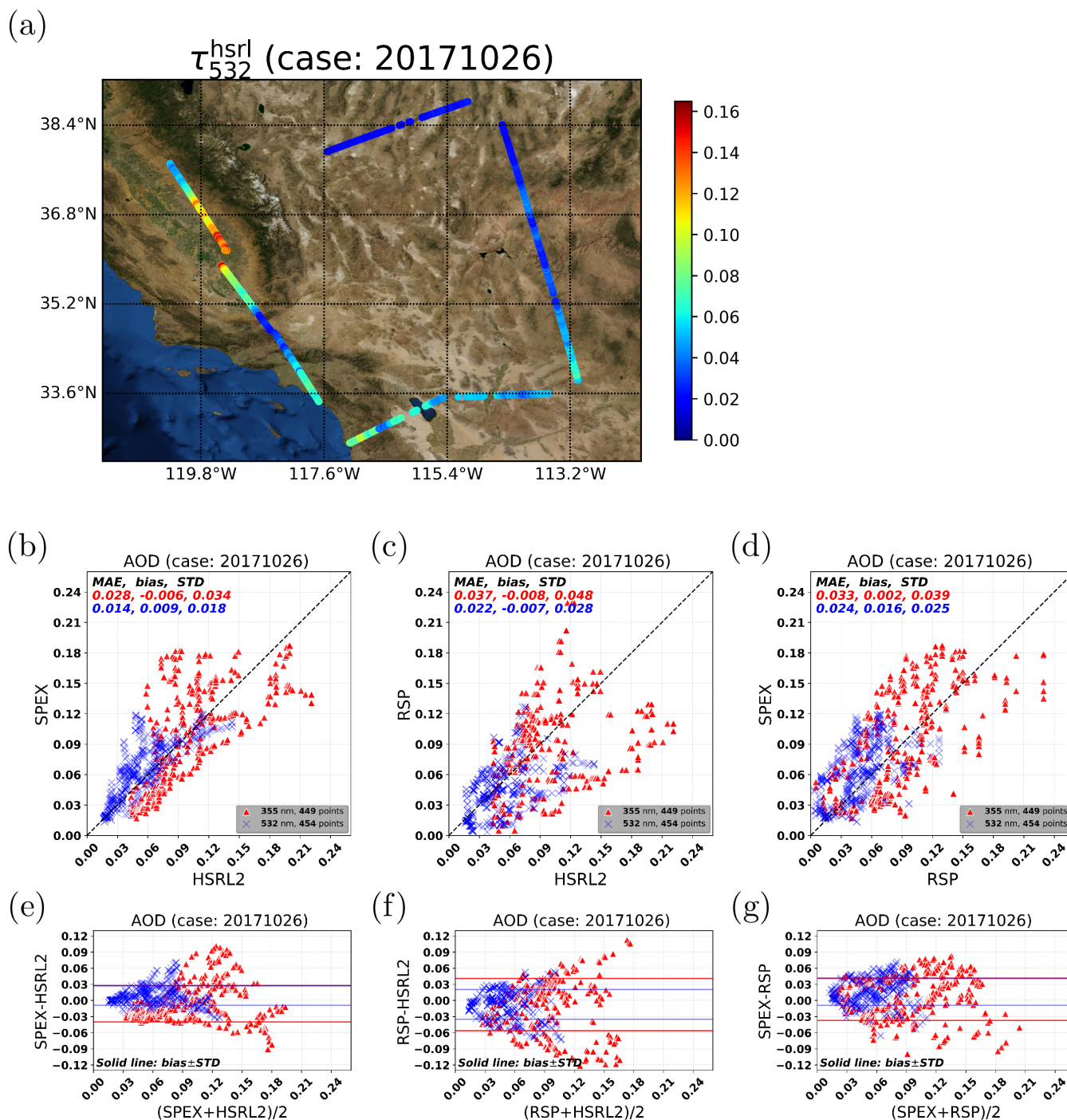
Figure 5. Comparison with HSRL-2 from 26 Oct 2017 (low AOD case) for AOD (355 nm and 532 nm) between SPEX and RSP retrievals. (a) HSRL-2 AOD colocation with SPEX and RSP. (The map is generated using python's basemap package and its arcgis image service 'ESRI_Imagery_World_2D'.) **(b)** SPEX AOD comparison with HSRL-2. **(c)** RSP AOD comparison with HSRL-2. **(d)** SPEX AOD comparison with RSP. **(e),(f),(g)** Bland-Altman plots for **(b),(c),(d)**, respectively.
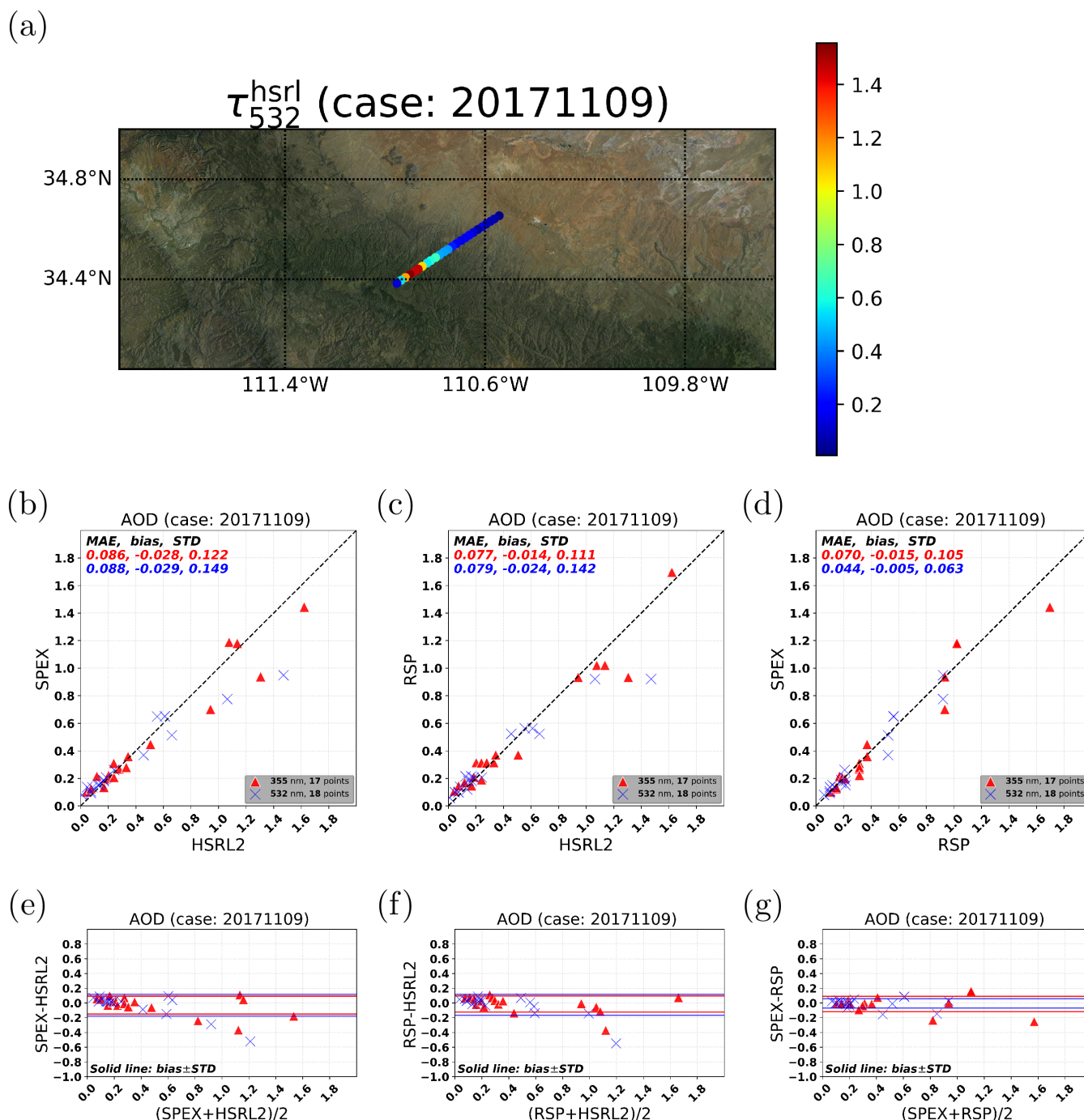
Figure 6. Comparison with HSRL-2 from 9 Nov 2017 (high AOD smoke case) for AOD (355 nm and 532 nm) between SPEX and RSP retrievals. (a) HSRL-2 AOD colocation with SPEX and RSP. (The map is generated using python's basemap package and its arcgis image service 'ESRI_Imagery_World_2D'.) **(b)** SPEX AOD comparison with HSRL-2. **(c)** RSP AOD comparison with HSRL-2. **(d)** SPEX AOD comparison with RSP. **(e),(f),(g)** Bland-Altman plots for **(b),(c),(d)**, respectively.
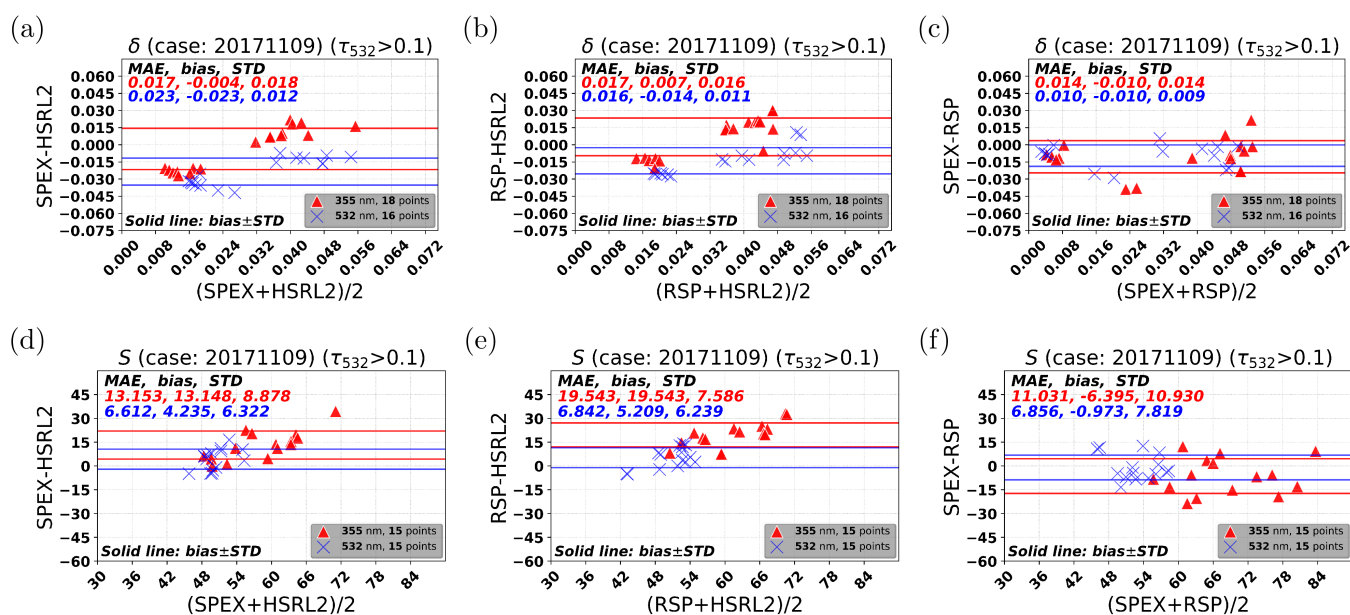
Figure 7. Comparison with HSRL-2 from 9 Nov 2017 (high AOD smoke case) for the aerosol depolarization ratio (δ) and the aerosol lidar ratio (S) between SPEX and RSP retrievals. (a) SPEX δ comparison with HSRL-2. **(b)** RSP δ comparison with HSRL-2. **(c)** SPEX δ comparison with RSP. **(d)** SPEX S comparison with HSRL-2. **(e)** RSP S comparison with HSRL-2. **(f)** SPEX S comparison with RSP.

Table 1. Definition of the effective radius (r_{eff}) and the effective variance (v_{eff}) in the SRON 5-mode retrieval.

	Mode 1	Mode 2	Mode 3	Mode 4	Mode 5
r_{eff} (µm)	0.094	0.163	0.282	0.882	1.759
v_{eff}	0.130	0.130	0.130	0.284	1.718

Table 2. Mean properties of the smoke plume for SPEX and RSP when AOD > 0.2 at 532 nm.

	SPEX	RSP
Fine mode real part of refractive index ($m_{\mathrm{r},532}^{\mathrm{f}}$)	1.579	1.556
Fine mode imaginary part of refractive index ($m_{\mathrm{i},532}^{\mathrm{f}}$)	0.038	0.036
Fine mode effective radius ($r_{\mathrm{eff}}^{\mathrm{f}}$)	0.116	0.119
Fine mode AOD (τ_{532}^{f})	0.554	0.509
Coarse mode AOD (τ_{532}^{c})	0.016	0.040
Aerosol layer height (ALH) (km)	4.417	1.585
SSA (ω_{532})	0.815	0.829
Fraction of spherical particles (f_{sphere})	0.989	0.846